**Forschungszentrum Karlsruhe**
in der Helmholtz-Gemeinschaft

**Wissenschaftliche Berichte**
FZKA 7415

# Disturbances Produced by an Electric Potential Probe on MHD Flows in Rectangular Ducts

**C. Mistrangelo, L. Bühler**

**Institut für Kern- und Energietechnik**
**Programm Kernfusion**

**Oktober 2009**

Forschungszentrum Karlsruhe

in der Helmholtz Gemeinschaft

Wissenschaftliche Berichte

FZKA 7415

# Disturbances produced by an electric potential probe on MHD flows in rectangular ducts

C. Mistrangelo, L. Bühler

Institut für Kern- und Energietechnik
Programm Kernfusion

Forschungszentrum Karlsruhe GmbH, Karlsruhe
2009

Für diesen Bericht behalten wir uns alle Rechte vor

Forschungszentrum Karlsruhe GmbH
Postfach 3640, 76021 Karlsruhe

Mitglied der Hermann von Helmholtz-Gemeinschaft
Deutscher Forschungszentren (HGF)

ISSN 0947-8620

urn:nbn:de:0005-074151

# Disturbances produced by an electric potential probe on MHD flows in rectangular ducts

## Abstract

Experimental data for local velocity in liquid metal duct flows exposed to an external magnetic field can be obtained from measurements of electric potential differences recorded by probes that are moved along the channel width. These instruments, known as conduction anemometers or Liquid-metal Electromagnetic Velocity Instruments (LEVI), have been used in the past preferentially for investigating almost fully developed magnetohydrodynamic (MHD) flows in poorly conducting ducts and flows with smooth variations along the channel axis. For such applications, where electric current density is negligible, the probe was assumed to give reliable results and the potential gradient signal was directly interpreted as a velocity measure. If the flow varies along its path on very short length scales, like in ducts with abrupt change of cross section or in manifolds, non-negligible 3D electric currents occur so that the LEVI readings may become inaccurate. Moreover, the presence of the probe itself may perturb significantly the flow field due to the formation of internal layers that develop along magnetic field lines tangential to the shaft and the insulating body of the instrument.

Experiments showed an asymmetry in the distribution of the measured transverse potential gradient and its underestimation compared with the one expected from flow rate measurements and from theoretical predictions for fully developed MHD flows.

A numerical analysis of MHD flows around a probe inserted in a rectangular duct has been performed to support the physical interpretation of potential measurements and to study and quantify the influence of the instrument itself on the readings. A calibration procedure is suggested, which allows using measurements of potential differences to get reliable data for velocities in the duct.

# Störungen von MHD Strömungen in rechteckigen Kanälen durch eine elektrische Potential-Sonde

## Zusammenfassung

Aus Messungen elektrischer Potentialdifferenzen mittels einer elektrischen Potentialsonde können experimentelle Daten für lokale Geschwindigkeiten von Flüssigmetall-Strömungen in einem homogenen Magnetfeld ermittelt werden. Potentialsonden, auch bekannt als "Conduction Anemometers" oder "Liquid-metal Electromagnetic Velocity Instruments" (LEVI), wurden in der Vergangenheit bevorzugt verwendet, um nahezu eingelaufene magnetohydrodynamische (MHD) Strömungen in schlecht leitenden Kanälen zu untersuchen, oder Strömungen, die sich entlang der Kanalachse nur schwach ändern. Für solche Anwendungen, bei denen elektrische Ströme vernachlässigbar sind, kann man davon ausgehen, dass die Sonde zuverlässige Ergebnisse liefert und der gemessene Potentialgradient direkt als ein Geschwindigkeitsmaß interpretiert werden kann. Wenn sich die Strömung auf sehr kleinen Längenskalen ändert, wie z.B. in Geometrien mit abrupten Änderungen des Querschnitts, sind jedoch dreidimensionale elektrische Ströme nicht mehr vernachlässigbar klein, so dass LEVI Messwerte ungenau werden können. Darüber hinaus kann die Anwesenheit der Sonde selbst bereits starke Störungen des Strömungsfelds verursachen, da sich interne Schichten entlang magnetischer Feldlinien tangential zum Schaft und zur Sonde ausbilden. Dieses Phänomen stört die Strömungsverteilung nicht nur in der Nähe der Sensorenspitzen sondern eventuell auch im ganzen Kanalquerschnitt.

Experimente zur Untersuchung von MHD-Strömungen in rechteckigen Kanälen mit einer plötzlichen Querschnittserweiterung zeigten, dass die Verteilung des gemessenen Potentialgradienten asymmetrisch ist und die Messwerte im Vergleich zu theoretischen Vorhersagen für voll entwickelte MHD-Strömungen kleiner sind. Eine numerische Untersuchung der Umströmung einer Sonde in einem rechteckigen Kanal wurde durchgeführt, um die physikalische Interpretation der Potentialmessungen zu untermauern und den Einfluss der Sonde auf die Messwerte zu quantifizieren. Zur Bestimmung von zuverlässigen Geschwindigkeitsdaten ausgehend von den aufgezeichneten elektrischen Potentialdifferenzen wurde ein Kalibrierungsverfahren definiert.

# Disturbances produced by an electric potential probe on MHD flows in rectangular ducts

## Contents

**1 Introduction** **1**

**2 Formulation of the problem** **3**

**3 Experimental set-up and instrumentation** **5**

**4 Operating principle of potential probes** **7**

**5 Measured quantities** **8**

**6 Computational method** **9**

**7 Results and discussion** **11**
- 7.1 Experimental observations . . . . . . . . . . . . . . . . . . . . . . . . . . 11
  - 7.1.1 Underestimation of potential gradient . . . . . . . . . . . . . . 11
  - 7.1.2 Asymmetry of measured potential gradient . . . . . . . . . . . 15
- 7.2 Interpretation of experiments by numerical simulations . . . . . . . . 15
  - 7.2.1 Underestimation of potential gradient . . . . . . . . . . . . . . 15
  - 7.2.2 Asymmetry of measured potential gradient profiles . . . . . . 20
  - 7.2.3 Extent of perturbed region around the probe . . . . . . . . . . 31
- 7.3 Calibration of experimental data . . . . . . . . . . . . . . . . . . . . . . 33

**8 Conclusions** **38**

**References** **40**

# 1 Introduction

An experimental campaign has been carried out in the MEKKA laboratory of the Forschungszentrum Karlsruhe to study the effects of an applied magnetic field on the flow of an electrically conducting fluid in geometries relevant for applications in fusion reactor blankets. Here circulating liquid metals are used as fuel-breeder and coolant. Their interaction with the strong magnetic field that confines the plasma induces electric currents in the fluid, which give rise to electromagnetic forces. These latter modify the velocity and pressure distributions in the ducts compared to those in hydrodynamic flows. The detailed knowledge of the established magnetohydrodynamic (MHD) flow is required to address the feasibility of proposed designs for fusion blankets (Morley, Malang and Kirillov (2005)). Moreover, as a basis for the validation of numerical codes for simulating this type of flows, experimental data for velocity are indispensable. The reliability of the latter ones is strongly related to the availability of appropriate measuring techniques. Indications about the proper numerical resolution of typical MHD phenomena like the flow in cores, in thin boundary layers or in internal parallel layers is obtained by comparing the computational results with local flow quantities measured inside the fluid.

Accurate measurements of local velocity in liquid metal MHD flows require special instrumentation both due to the physical characteristics of the fluid (opaque, chemically aggressive and often at high temperature) and to the presence of a magnetic field. In the following a brief survey of various approaches used to record velocity in liquid metals is given. A historical overview of velocity measurement techniques for liquid metal flows as well as a description of their limitations and applicability can be found in Eckert, Cramer and Gerbeth (2007).

In the past, velocity features in MHD flows have been determined for instance by using Pitot tubes. However, it has been noticed that the local pressure is in general a function of the magnetic field magnitude (Branover, Gel'fgat, Tsinober, Shtern and Shcherbinin (1966)), requiring therefore particular calibration and corrections (Hunt and Malcolm (1968)). Moreover, problems can occur due to metal solidification within pressure gauge tubes. Hot wire anemometers have also been employed (Sajben (1965), Platnieks and Uhlmann (1984)), but difficulties arise both from the chemical reactivity of the fluids that limits the duration of the sensor and from the large thermal conductivity of liquid metals and the high temperatures. Another method to determine local velocities in liquid metal flows is recording the electric field induced by the motion of the electrically conducting fluid in a magnetic field, which is measurable as electric potential differences between two or more thin sensor tips located at the top of a probe. The magnetic field can be created either locally at the instrument tip by a miniature permanent magnet embedded in the probe itself ( Ricou and Vives (1982), Weissenfluh (1985)), or globally, over the entire flow, by an external magnetic system, as always present in MHD experiments (Kit, Kolesnikov, Tsinober and Shtern (1969)). Electric potential probes, known as Conduction Anemometers or Liquid-metal Electromagnetic Velocity Instruments (LEVI), have been proposed early by Williams (1930) who suggests introducing in the moving fluid "searching electrodes" to determine the electromotive forces induced by the magnetic field. Kolin (1943, 1944) proposes a probe that consists of two fine wires, referred to as "exploring electrodes", which are insulated except at the tips and they are separated by a distance of the order of "a few thousandths of an inch". By means of this sensor the components of the local potential gradient can be recorded. They can be interpreted in terms of velocity components in the plane perpendicular to the applied magnetic field if some basic requirements, related to the magnitude of induced circulating currents, are met. A detailed description of these probes and their operation is given in Sect.4. Potential difference probes have been extensively used to measure mean and fluctuating characteristics of MHD turbulent flows (Kit (1970)), both in the case of two-dimensional turbulence (Kolesnikov and Tsinober (1972)) and for engineering applications in fusion technology (Burr, Barleon, Müller and Tsinober (2000)).

Usually one pair of sensor electrodes is used per each component of potential gradient, as described e.g. in Kit et al. (1969), Reed, Picologlou, Dauzvardis and Bailey (1986), Andreev, Kolesnikov and Thess (2007), but even four tips are enough to determine entirely the three components of the potential gradient (Burr et al. (2000)). Probes with five and seven tips have been used for the determination of field aligned vorticity as reported by Votsish and Kolesnikov (1976), Tsinober, Kit and Teitel (1987).

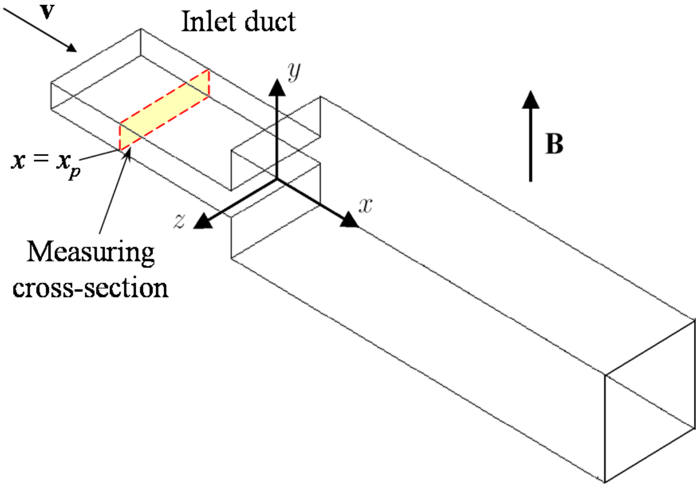

Figure 1: Geometry considered in the experimental and numerical studies. The present analysis focuses on data recorded in the flat inlet rectangular duct, in a cross section positioned at $x_p$, at sufficient distance from the sudden expansion. The probe moves on the horizontal symmetry plane and its tip is located at $P(x_p, 0, z_c)$. Here $z_c$ is the transverse position of the center of the head of the sensor.

Recent measurements of electric potential differences in MHD flows in an electrically conducting flat rectangular duct performed by using a LEVI showed an asymmetry in the distribution of the measured transverse potential gradient and its systematic underestimation compared with values expected from flow rate measurements (Bühler and Horanyi (2006)). A review of measured data presented e.g. in Hunt and Stewartson (1969), Picologlou, Reed, Dauzvardis and Walker (1986), Reed et al. (1986), Burr (1998) confirms that experimentally determined velocities obtained by potential difference probes are often smaller than results from mass flow measurements or theory. Some authors suggested that defects in a proper sensor reading could be related to locally induced electric currents (Kolin and Reiche (1954), Shercliff (1962), Korsunskii (1975)).

In this report numerical results for three-dimensional MHD flows around a probe are compared with experimental data to estimate the influence of the instrument on the flow pattern and to quantify the perturbation that the presence of the probe imposes on the flow. The computational data are used to support the physical interpretation of the potential difference measurements and to determine, when required, a suitable scaling procedure that allows using the recorded potential gradient as a measure for velocity components. The discussed numerical results consider MHD flows in a rectangular duct that represents the inlet channel of a larger test section (see Fig.1) used to investigate MHD flows in sudden expansions (Horanyi, Bühler and Arbogast (2005)). In the last section of the paper a suitable scaling of recorded potential differences is suggested.

## 2 Formulation of the problem

We consider the three-dimensional steady state flow of an incompressible, viscous, electrically conducting fluid exposed to a uniform transverse magnetic field. The problem is described by the full set of stationary non-linear, inertial, inductionless MHD equations accounting for the conservation of momentum and mass, which in non-dimensional form read as

$$\frac{1}{N}\left(\mathbf{v}\cdot\nabla\right)\mathbf{v} = -\nabla p + \frac{1}{Ha^2}\nabla^2\mathbf{v} + \mathbf{j}\times\mathbf{B}, \tag{1}$$

$$\nabla\cdot\mathbf{v} = \mathbf{0}. \tag{2}$$

The electric current density is determined through Ohm's law

$$\mathbf{j} = -\nabla\phi + \mathbf{v}\times\mathbf{B}, \tag{3}$$

under the constraint of charge conservation

$$\nabla\cdot\mathbf{j} = 0. \tag{4}$$

By taking the divergence of Ohm's law, with condition (4), a Poisson equation for the electric potential is obtained:

$$\nabla^2\phi = \nabla\cdot\left(\mathbf{v}\times\mathbf{B}\right). \tag{5}$$

In these equations the variables $\mathbf{v}$, $p$, $\mathbf{B} = \hat{\mathbf{y}}$, $\mathbf{j}$ and $\phi$ denote velocity, pressure, magnetic field, current density and electric potential, scaled by the reference quantities $v_0$, $p_0 = \sigma v_0 L B_0^2$, $B_0$, $j_0 = \sigma v_0 B_0$ and $\phi_0 = v_0 L B_0$, respectively. The quantity

$B_0$ represents the magnitude of the externally applied homogeneous magnetic field. Fluid properties like electric conductivity $\sigma$, kinematic viscosity $\nu$ and density $\rho$ are assumed to be constant. In order to be consistent with previous analyses (Bühler and Horanyi (2006) and Mistrangelo (2005)), the average velocity in the large outlet square channel of the expanding test section is chosen as velocity scale $v_0$. With this scale the mean non-dimensional velocity in the large duct becomes $\bar{v} = 1$ while that in the small one is $\bar{v} = 4$. As characteristic length scale the half width of the duct, $L = 47$ mm, has been chosen, so that the non-dimensional size of the flat inlet duct is $-0.25 \leqslant y \leqslant 0.25$ and $-1 \leqslant z \leqslant 1$, measured along magnetic field lines and in transverse direction, respectively (see Sect.3, Fig.2 for details). Instead the size of the large outlet channel along magnetic field lines is $-1 \leqslant y \leqslant 1$. For liquid metals, as used in the discussed experiments, the magnetic Reynolds number is usually small ($Re_m = \mu\sigma L v_0 << 1$, where $\mu$ is the magnetic permeability), i.e. the magnetic field induced by currents in the fluid is negligible compared to the imposed one. In other words, the applied magnetic field is not affected by the motion of the electrically conducting medium.

The dimensionless groups in (1) are the Hartmann number and the interaction parameter

$$Ha = B_0 L \sqrt{\frac{\sigma}{\rho\nu}}\ , \qquad N = \frac{\sigma L B_0^2}{\rho v_0}\ . \tag{6}$$

The square of the Hartmann number represents the relative importance of electromagnetic forces compared to the viscous ones; the interaction parameter gives instead a measure of the ratio between electromagnetic and inertia forces. The hydrodynamic Reynolds number is related to these groups through the relation $Re = Ha^2/N$.

In the present study the walls of the channel have finite thickness $t_w$ and finite electric conductivity $\sigma_w$. As a consequence, part of the current flowing in the fluid may close its path in the walls. Therefore, the following equations have to be solved simultaneously in the solid domain:

$$\mathbf{j}_w = -\frac{\sigma_w}{\sigma}\nabla\phi_w, \qquad \nabla\cdot\mathbf{j}_w = 0. \tag{7}$$

At the fluid-solid interface the kinematic no-slip condition ($\mathbf{v} = 0$) applies together with continuity of electric potential ($\phi = \phi_w$) and wall-normal component of current density ($\mathbf{j}\cdot\mathbf{n} = \mathbf{j}_w\cdot\mathbf{n}$). The last two conditions state that the potential $\phi_w$ at the wall equals the potential $\phi$ in the fluid, i.e. no contact resistance is present, and the current density in the wall $\mathbf{j}_w$ and in the fluid $\mathbf{j}$ have the same normal component. The wall potential is determined by the currents flowing in the wall. Here the essential parameter is the wall conductance ratio

$$c = \frac{\sigma_w t_w}{\sigma L}. \tag{8}$$

The surrounding environment is assumed to be non conducting so that currents cannot leave the walls through their external surface, where therefore the normal component of the electric current vanishes ($\mathbf{j}\cdot\mathbf{n} = 0$).

# 3 Experimental set-up and instrumentation

The experimental data discussed in the present report have been measured in the MEKKA liquid metal loop at the Forschungszentrum Karlsruhe. An eutectic sodium-potassium alloy $Na^{22}K^{78}$ is used as working fluid. Its melting point at $-12.6$ °C (Foust (1972)) allows operating the loop at room temperature. Due to the high electric conductivity ($\sigma_{\mathrm{NaK}} = 2.88 \cdot 10^6\ \Omega^{-1}\mathrm{m}^{-1}$ at 20 °C) and low density ($\rho_{\mathrm{NaK}} = 868.2$ kg $\mathrm{m}^{-3}$ at 20 °C) of this liquid metal, the experiments can be run in a range of parameters close to that relevant for fusion applications, while using magnetic fields that are about three times smaller than those in fusion reactors. In this way the experimental results obtained by using a model geometry can be transferred to real applications according to the principle of dynamic similarity. The employed test section (Fig.1) has been manufactured from stainless steel that has electric conductivity $\sigma_w = 1.26 \cdot 10^6\ \Omega^{-1}\mathrm{m}^{-1}$ (Stahl-Eisen-Werkstoffblätter (SEW 310) (1992)) and the walls have a thickness $t_w = 3$ mm. According to (8), considering the conductivity $\sigma_{\mathrm{NaK}}$ of the NaK, the wall conductance parameter in the experiments is $c \simeq 0.03$.

In the laboratory a liquid metal inventory of about 200 l is available and the fluid is circulated by mechanical and electromagnetic pumps depending on the needed velocity. Flow rates up to 25 $\mathrm{m}^3$/h and pressure heads up to 9 bar can be reached. In order to evaluate the characteristic flow parameters during experiments an accurate knowledge of the flow rate in the loop is required. For this reason a gyrostatic- and an electromagnetic flow meter are inserted in series in the loop to measure the flow rate. The homogeneous magnetic field in which the test section is placed has a maximum value of 2.1 T in a volume of $170 \times 480 \times 800\ \mathrm{mm}^3$. A detailed description of the MEKKA facility can be found in Barleon, Mack and Stieglitz (1996).

The electric potential probe used in the experiments (Fig.2) consists of a Degussit ceramic body with external diameter of 1.55 mm that has 4 bores in which 4 sensing wires with diameters of 0.2 mm are inserted. The body becomes thicker after covering it with insulating varnish, reaching a thickness of 1.8 mm. The sensing wires are also lacquered to make their surface insulating and electric contact is ensured at the tips. The probe has been manufactured to measure all three components of potential gradient for general applications, however in the present work only tips $a$ and $b$ have been used to record the only non-zero transverse component. These measuring points are located 4 mm upstream of the probe body and they are separated by a distance of 1.2 mm. The insulating head of the probe is fixed to an electrically conducting holder of 6 mm diameter. This latter can be moved transversely across the channel by means of a PC - controlled mechanism driven through a long rotating axis by a stepping motor located outside the magnetic field, which allows precise positioning of the sensor (Fig. 3). A sketch of the instrument inside the channel is shown in Fig.2b, c. The coordinate reference system has been chosen so that the $x$ axis coincides with the main flow direction, the top of the insulating body of the probe is located at $x = 0$ and the magnetic field is aligned with $y$ ($\mathbf{B} = \hat{\mathbf{y}}$). The traversable sensor has been inserted at different axial positions along the test section in order to obtain data for local potential and potential gradients inside the channel. The signals for potential difference have been measured through a remotely controlled multi-channel nano-voltmeter with a physical integration time of 2 s.

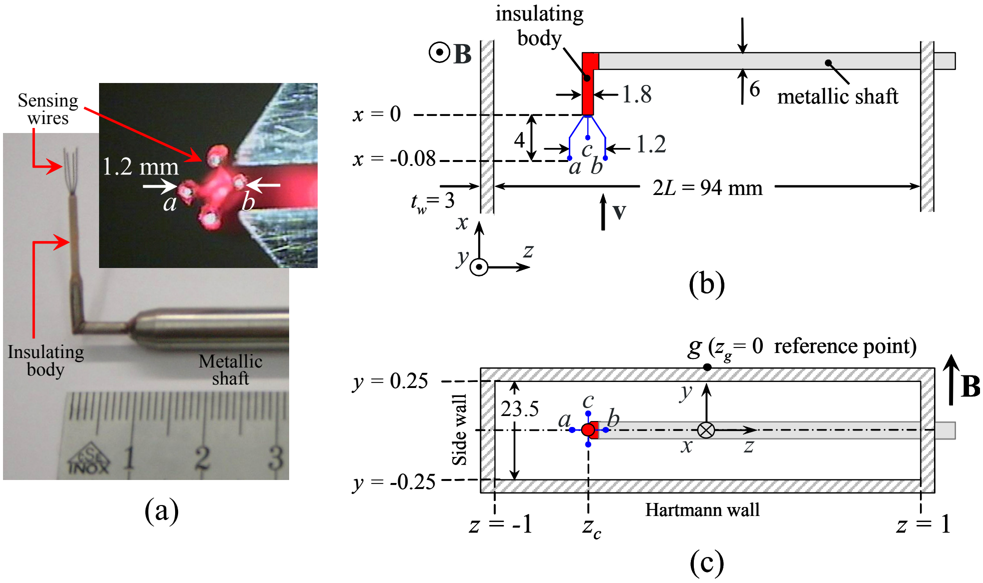
Sensing wires
1.2 mm
a
b
Insulating body
Metallic shaft
1
2
3
insulating body
⊙B
1.8
6
metallic shaft
x = 0
4
1.2
c
x = -0.08
a b
$t_w$= 3
2L = 94 mm
v
x
y
z
g ($z_g$= 0 reference point)
y = 0.25
23.5
c
a
b
y
B
Side wall
x
z
y = -0.25
Hartmann wall
z = -1
$z_c$
z = 1

(a)

(b)

(c)

Figure 2: (a) Picture of the probe used for the experiments. The enlarged view shows the head of the sensor and the sensing wires covered with the red insulating lacquer. (b)(c) Sketch of an electric potential probe inserted into a rectangular duct: view perpendicular to **B** and in a cross-section. The distance between the sensing tips of the probe and their length are enlarged in the sketch to show details of the geometry.

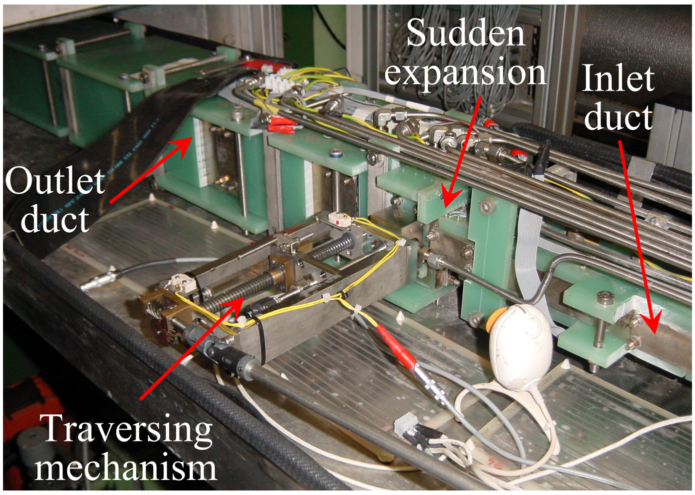
Sudden expansion
Inlet duct
Outlet duct
Traversing mechanism

Figure 3: Traversing mechanism for movable potential probes here positioned at the expansion. On the top of the test section pipes for pressure measurements are present. The insulating green plates are the support for the spring loaded probes used to measure surface potential.

# 4 Operating principle of potential probes

Figure 4 shows a typical MHD velocity profile in an electrically conducting rectangular duct, for sufficiently intense imposed magnetic field (large $Ha$). This is the velocity distribution we want to measure during the discussed experiments. It is characterized by a uniform core and high velocity jets in the boundary layers that form along the walls parallel to the magnetic field which are named side walls ($z = \pm 1$). The side layer thickness scales as $\delta_S \sim Ha^{-1/2}$. Thinner boundary layers ($\delta_H \sim Ha^{-1}$), called Hartmann layers, are present at the walls ($y = \pm 0.25$) where the magnetic field has a normal component. The described characteristics of the MHD duct flow clearly highlight the need of a high spatial resolution of the recorded potential gradient in the side layers, i.e. the probe has to be moved with small steps in these regions.

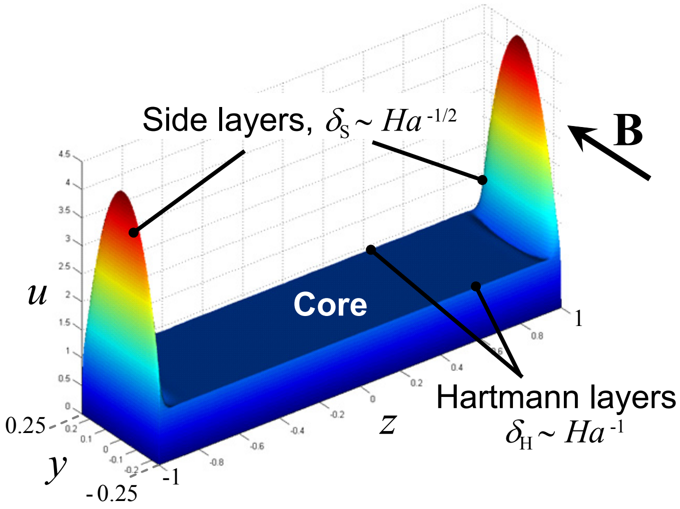

Figure 4: Typical MHD velocity distribution in an electrically conducting rectangular duct with high aspect ratio. In the boundary layers, at walls parallel to the magnetic field, velocity jets are present. In the duct core the velocity is uniform.

The operating principle of an electric potential difference probe is based on Ohm's law (3), which allows expressing the velocity components in a plane perpendicular to the homogeneous magnetic field $\mathbf{B} = \hat{\mathbf{y}}$ as

$$\mathbf{v}_\perp = \left(\frac{\partial \phi}{\partial z} + j_z\right)\hat{\mathbf{x}} + \left(-\frac{\partial \phi}{\partial x} - j_x\right)\hat{\mathbf{z}}. \tag{9}$$

This expression shows that the local velocity is determined not only by the potential gradient but also by the currents induced in the fluid. Therefore, the potential difference measured at the sensor tips can be directly interpreted in terms of local velocity only if the current density is very small or known (Kolin and Reiche (1954), Branover, Gel'fgat, Kit and Tsinober (1970), Tsinober et al. (1987)). Non negligible transverse current density $j_z$ may appear both in fully developed and 3D MHD flows.

Instead, axial currents $j_x$ occur only in the latter case and they can be driven for instance by an axial potential gradient, as in the case of MHD flows in expansions, or they are caused by the presence of the measuring sensor itself.

The electric current density for fully developed high Hartmann number MHD flows in insulating ducts or in ducts with thin conducting walls ($c \ll 1$) is typically of the order $O\left(c + Ha^{-1}\right) \ll 1$. It should be therefore negligible in Ohm's law (3) in comparison with terms of order unity, i.e. the potential gradient $\nabla\phi$ and the induced electric field $\mathbf{v} \times \mathbf{B}$. This fact permits to simplify expression (9) so that the velocity $\mathbf{v}_\perp$ can be determined as

$$\mathbf{v}_\perp = u\hat{\mathbf{x}} + w\hat{\mathbf{z}} \approx -\left(\nabla\phi \times \hat{\mathbf{y}}\right) = \frac{\partial\phi}{\partial z}\hat{\mathbf{x}} - \frac{\partial\phi}{\partial x}\hat{\mathbf{z}} \tag{10}$$

if the components of the electric potential gradient in a plane perpendicular to $\mathbf{B}$ are measurable.

# 5 Measured quantities

In the experiments the approximate local transverse potential gradient $\partial\phi/\partial z \approx \Delta\phi/\Delta z$ has been measured by considering the potential at tips $a$ and $b$ (Fig.2), which are separated by a normalized distance $d = z_b - z_a$. The local value of the electric potential $\phi(z_a)$ is given instead by the difference between the potential at tip $a$ and the one at a reference position $g$ at the symmetry plane $z = 0$ on the upper wall normal to the magnetic field (Fig.2c). Thus the quantities recorded during the experimental campaign are:

$$\frac{\Delta\phi}{\Delta z} = \frac{\phi_b - \phi_a}{d}, \qquad \phi(z_a) = \phi_a - \phi_g. \tag{11}$$

The transverse potential gradient $\partial\phi/\partial z$ has been also evaluated by differentiation with respect to $z$ of the potential $\phi(z)$ recorded at a large number of positions $z_i$:

$$\left.\frac{\partial\phi}{\partial z}\right|_{i+1/2} \approx \frac{\phi\left(z_{i+1}\right) - \phi\left(z_i\right)}{\Delta z}. \tag{12}$$

Near the side layers along walls parallel to the imposed magnetic field, where the highest velocities and potential gradients are present (see Fig.4), measurements have been taken with small steps $\Delta z = z_{i+1} - z_i = 0.1 \div 0.2$ mm to have a high and adequate resolution. The transverse step size has been increased progressively towards the center of the duct up to 2 mm. Here, in the core, a uniform velocity distribution is expected. As a result, the evaluation of the potential gradient $\partial\phi/\partial z$ from the experimental data $\phi(z)$ recorded near the side wall can lead to values with a large scattering since even slight measuring uncertainties in the recorded local potential are amplified when divided by the very small $\Delta z$ (Bühler, Horanyi and Mistrangelo (2008)). Therefore, in order to get a better representation of the gradient $\partial\phi/\partial z$ a smooth analytical fit $\phi_{fit}(z) = Fit(\phi_i)$ of the locally measured potential has been defined whose derivative $\partial\phi_{fit}/\partial z$ is considered for the analysis of the experimental data.

| **Electric potential** | |
|---|---|
| $\phi_i = \phi_a(z_i) - \phi_g$ | measured local value at $z_i$ |
| $\phi_{fit}(z) = Fit(\phi_i)$ | analytical fit of recorded $\phi_i$ |
| | |
| **Potential gradient** | |
| $\frac{\Delta\phi}{d} = \frac{\phi_b - \phi_a}{\Delta z}$ | measured approximate value |
| $\frac{\partial \phi_{fit}}{\partial z}$ | differentiation of the fit $\phi_{fit}$ |

Table 1: Measured and evaluated values for the electric potential and its gradient.

Table 1 summarizes the quantities that have been used to analyze the distribution of the electric potential and its gradient in the investigated MHD duct flows. In the following we will focus on the comparison between the approximate potential gradient $\Delta\phi/d$ and the gradient $\partial\phi_{fit}/\partial z$ of the smooth analytical fit.

# 6 Computational method

Numerical simulations of 3D MHD flows in a rectangular duct containing an electric potential probe have been performed for evaluating the influence of the measuring instrument on the velocity and potential distribution. Calculations have been carried out by using a modified version of the commercial code CFX − 5.6 which is based on the finite volume method and on a modified form of the SIMPLE algorithm for pressure-velocity coupling to ensure mass conservation (Patankar (1980)). Fortran user subroutines have been developed to include the additional terms and equations required to describe and simulate MHD flows. The electromagnetic force has been introduced as a source term in the momentum equation (1) and a Poisson equation (5) has been solved for the electric potential.

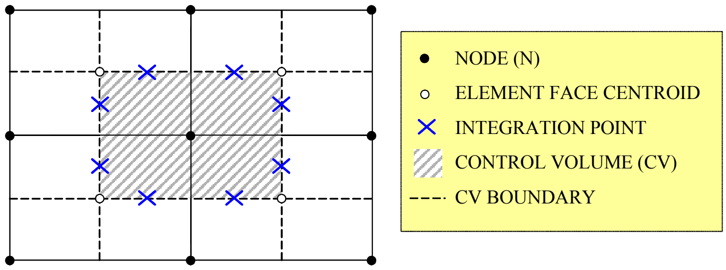

Figure 5: Sketch of a control volume in the computational domain and characteristic points used for solving the equations.

More in details, for solving the equations the grid in Fig.5 is used. Interpolation is performed to locate the solution of the pressure and velocity fields at the same nodal positions. A coupled solver is employed such that the full system of equations is solved simultaneously across all grid nodes. All the solution variables and fluid properties are stored at the element nodes, surface fluxes are discretely represented at the integration points. In order to calculate the variation of the solution within an element shape functions are used. Concerning the coupling between potential and Navier-Stokes equations, first a starting value of the induced electric field $\mathbf{v} \times \mathbf{B}$ is calculated and interpolated to the integration points to get the surface flux $\nabla \cdot \mathbf{j}$ used as source term in the Poisson equation (5) for the electric potential. Then the total current density is evaluated by Ohm's law (3) and used to calculate the Lorentz force $\mathbf{j} \times \mathbf{B}$ in the momentum equation (1). The discrete system of linearized equations is then solved by an iterative procedure.

Convergence of the solution is judged both considering the value of the residuals and by monitoring the solution variables at fixed significant locations in the computational domain. The discussed results are those reached when all the root mean square residuals are smaller than $10^{-5}$ and the variables at the monitored locations remain constant. The final numerical tool has been accurately validated by comparison with analytical solutions, results present in literature and experimental data ( Mistrangelo (2005)).

An aspect that has to be carefully considered in CFD simulations is the mesh used to discretize the computational domain. It is important to resolve properly the geometric features that affect the flow and the regions where the largest gradients of the variables occur, such as the boundary and internal layers. In the present case boundary layers develop both at the channel walls and at the probe surfaces. Internal layers spread across the fluid along the magnetic field lines that are tangential to the edges of the probe body. By increasing the Hartmann number, namely the magnetic field strength, the thickness of these layers decreases. Therefore the need of resolving these regions adequately, while preserving the mesh quality, leads to a progressive rise in the total number of nodes. As a consequence, restrictions on the accuracy of the solution at high Hartmann numbers ($Ha > 1000$) are related to limitations in computer capabilities.

A grid sensitivity study has been performed to exclude possible non-physical effects related for instance to the asymmetry of the grid, which has to be refined not only in the boundary layers but also around the measuring instrument. Moreover, the proper resolution of these layers has been verified. These investigations showed that with a non-uniform mesh having a larger number of nodes in all the boundary and internal layers a grid-independent solution can be obtained.

According to the features of the probe used in the experiments (see Fig.2), the simulated geometry representing it consists of an insulating body parallel to the main flow direction, which has been modelled assuming for simplicity a square cross section. The body is fixed to a metallic shaft perpendicular to it, that crosses transversely the channel. This holder has been modelled as a full bar of steel without internal cavity, having a conductance ratio equivalent to that of a shaft with wall of finite thickness. Numerical simulations have been performed also including the four very thin sensing wires in the geometric model. Results show that their presence does not significantly affect the flow. The perturbation caused by the much larger sensor head is stronger and dominates the main characteristics of the flow at the probe top. Therefore, since the effects of the sensing wires on the flow are much smaller than the perturbations caused by the head of the probe, they have been omitted in the present analysis. We can also observe that the sensing wires have been manufactured from high quality steel to get the best strength. For that reason, we are confident that the flow does not influence their distance. Experimental results have confirmed this assumption.

In the performed numerical analysis various transverse $z$-positions of the probe and different values of the characteristic parameters $Ha$ and $N$ have been considered.

# 7 Results and discussion

## 7.1 Experimental observations

### 7.1.1 Underestimation of potential gradient

As already mentioned, the electric potential profiles, described in this work, were measured in the straight inlet rectangular duct, in the flat part of the employed test section (see Fig.1), in a region where the flow was fully developed. Three-dimensional MHD effects due to the expanding flow (Bühler (2008)) are located downstream at a distance large enough that they do not influence the flow under investigation. This has been verified by potential measurements on the duct surface. During the experimental campaign profiles of the electric potential $\phi(z)$ have been recorded along the channel width together with potential differences $\Delta\phi/d$ according to (11).

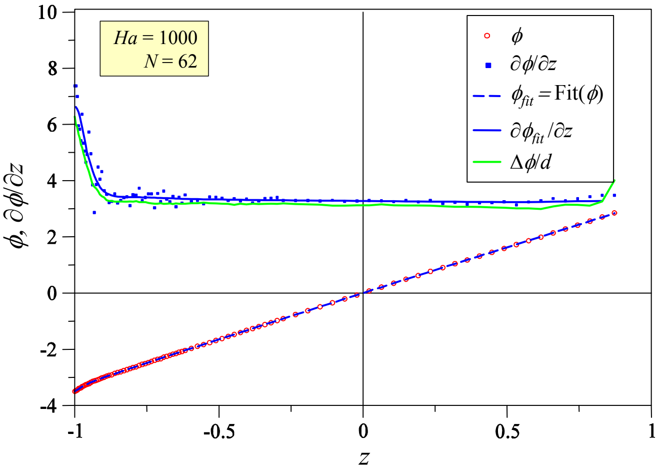

Figure 6: Profile of measured potential $\phi$ and its gradient $\partial\phi/\partial z$ compared with measurements of local approximate potential gradient $\Delta\phi/d$ for $Ha = 1000$ and $N = 62$. The curve $\phi_{fit}$ represents a smooth analytical fit of the measured potential data $\phi$ and $\partial\phi_{fit}/\partial z$ is its derivative.

Results of a measured potential profile $\phi(z_i) \equiv \phi$ at $Ha = 1000$ and $N = 62$ are shown in Fig.6 by open circles at positions $z_i$. In the center of the duct one can observe the well-known linear potential profile of a fully developed MHD flow in rectangular ducts with thin conducting walls. Slight deviations from this linear trend occur only in the side layer close to the wall at $z = -1$, which has an orientation parallel to the magnetic field. The other wall at $z = 1$ could not be reached by the probe because of geometrical restrictions of the driving mechanism. In Fig.6 the squares represent the potential gradient obtained by numerical differentiation of the measured potential $\phi_i$ as given by (12). As described in Sect.5, in the center of the duct, where the distance $\Delta z = z_{i+1} - z_i$ between two measuring locations is not too small, those results give a good indication of the transverse potential gradient. Near the side wall ($z = -1$), where $\Delta z$ was chosen very small for resolving properly the parallel boundary layer, slight measuring uncertainties in the potential $\phi$ lead to larger uncertainties in the potential gradient $\partial\phi/\partial z$ (12). This yields the evident scattering of the data for $\partial\phi/\partial z$ close to the side wall. The measured potential gradient is compared with the one $\partial\phi_{fit}/\partial z$ of the analytical fit of the recorded local potential. It is marked by the blue solid line in Fig.6. A comparison of this derivative with the approximated potential gradient $\Delta\phi/d$ (green solid line), obtained by measuring directly the potential difference between two tips of the probe, as described by (11), indicates good agreement, thus confirming the validity of the employed measuring principle.

Similar agreement is found also when reducing progressively the liquid metal flow rate, i.e. for larger interaction parameters e.g. $N = 125$, not explicitly shown here, and $N = 250$ in Fig.7a. Nevertheless, it can be observed that the approximate potential gradient $\Delta\phi/d$ is always smaller than $\partial\phi_{fit}/\partial z$. This deviation increases monotonically with the interaction parameter $N$, as shown in Fig.7b for $N = 500$. This difference reaches a magnitude that can not be ignored if one wants to use the probe reading $\Delta\phi/d$ as a measure for local axial velocity. This is visible in Fig.8 where results for $N = 1000$ are depicted. The fact that the underestimation is more expressed for high interaction parameters $N$ could be explained considering the action of inertia forces on the flow. When they are strong, i.e. for small interaction parameters ($N \leqslant 250$), they help to move the region of perturbation further downstream compared to the cases for large $N$, and eventually behind the location of the sensing wires. In that case we obtain very good readings of the instrument without the need of calibration. The discussed results are summarized in Fig.9a where the measured approximate transverse potential gradient is plotted along the duct width for a constant Hartmann number $Ha = 1000$ and various interaction parameters $N$. The value of $\partial\phi_{fit}/\partial z$ instead remains practically unchanged and in very good accordance with theoretical predictions for all the values of $N$ as expected for a fully developed MHD flow. This is shown in Fig.9b where the profile of the potential gradient obtained by differentiation of the analytical fit of the recorded electric potential is displayed for a constant Hartmann number $Ha = 1000$ and various interaction parameters $N$. In the core of the duct all the curves coincide. Instead, close to the side wall ($z = -1$), in the field-parallel boundary layer, by reducing $N$ the maximum potential gradient, hence the velocity, becomes smaller and the thickness of the side

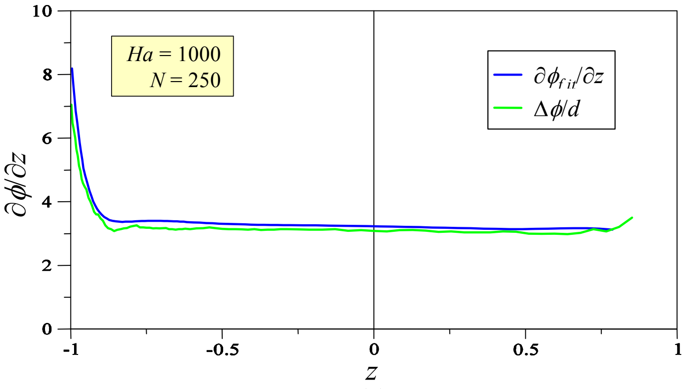

(a)

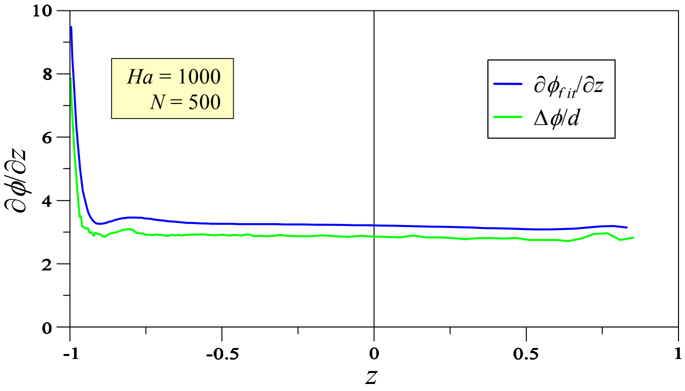

(b)

Figure 7: Profile of potential gradient $\partial\phi_{fit}/\partial z$ compared with recorded potential gradient $\Delta\phi/d$ for $Ha = 1000$, (a) $N = 250$ and (b) $N = 500$. By increasing $N$ the deviation between the two curves becomes larger.

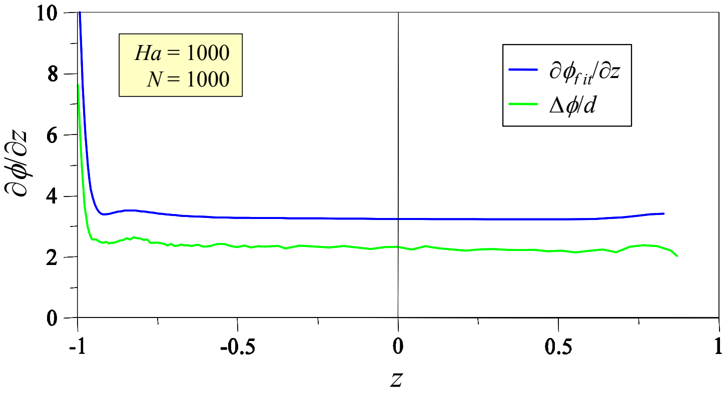

Figure 8: Profile of potential gradient $\partial\phi_{fit}/\partial z$ compared with the recorded one $\Delta\phi/d$ for $Ha = 1000$ and $N = 1000$.

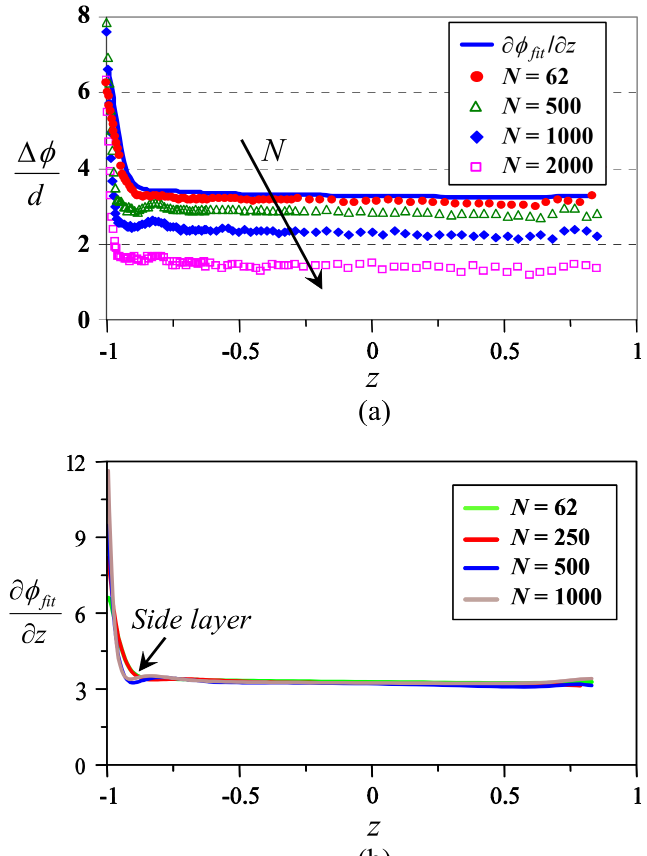

(a)

(b)

Figure 9: (a) Measured potential gradient $\Delta\phi/d$ for different interaction parameters $N$ and $Ha = 1000$ compared with the gradient of the analytical fit at $N = 62$. (b) Profiles of potential gradient obtained by differentiation of the analytical fit of the measured potential values, for $Ha = 1000$ and various $N$.

layer enlarges. This phenomenon can be explained in terms of onset of instabilities in the side layer and transition from laminar to turbulent flow regime. Studies of stability of side layers in MHD flow in rectangular ducts (Bühler and Horanyi (2009)) showed that for moderate Reynolds numbers, $Re \leqslant 2000$ ($N \geqslant 500$), the time-averaged velocity, determined through measurements of potential gradients, is characterized by a uniform core value and a strong increase close to the side wall as expected for laminar MHD flows in conducting rectangular channels ($N = 1000$, $N = 500$ in Fig.9b). In this range of parameters the recorded values of local potential gradient agree well with laminar theoretical predictions. When $Re > 2000$ ($N < 500$) the laminar flow becomes unstable and time dependent fluctuations are observed, which are confined to the near-wall region. As a result the side layer becomes thicker and the maximum velocity reduces compared to the laminar regime, as shown in Fig.9b by the profiles for $N = 250$ and $N = 62$. On the other hand, in spite of the systematic underestimation of the potential gradient by direct measurement of potential differences, qualitatively the profile $\Delta\phi/d$ agrees well with $\partial\phi_{fit}/\partial z$ so that the question arises about the reason for the $N$-dependent deviation and the need of careful calibration of the experimental results is envisaged.

### 7.1.2 Asymmetry of measured potential gradient

In addition to the underestimation of the potential gradient by direct measurement of potential differences, another phenomenon has been found by analyzing the experimental data. It has been noted that the potential gradient profiles are slightly asymmetric across the width of the channel (see e.g. Fig.9a) or, in other words, they are inclined towards the side wall ($z = 1$) through which the probe is inserted. The asymmetry increases with the intensity of the applied magnetic field, i.e. with the Hartmann number $Ha$. An inclination of the potential profile was observed also by Reed et al. (1986). These authors associate this fact with difficulties in removing uniformly the oxide layer that covers the internal surface of the test section, namely they explain it in terms of imperfect electrical wetting. In the present report the authors try to describe and justify the observed asymmetry of the measured potential gradient profile considering the occurrence of internal field-parallel layers and complex 3D current loops around the instrument (see Sect.7.2.2).

## 7.2 Interpretation of experiments by numerical simulations

In the following, results obtained from numerical simulations of 3D MHD duct flows around a probe are used to give a physical explanation of the before mentioned discrepancies observed in the experimental data. For simplicity the cylindrical body of the probe and its metallic holder are represented in the calculations with square cross-sections. The very thin sensing wires have not been included in the simulations (see Sect.6).

Numerical results have been obtained for the cases in which the probe is located in the centre of the duct at $z_c = 0$ and close to the side wall at $z_c = -0.79$, for a constant Hartmann number $Ha = 1000$ and for various interaction parameters $N$, as used in the experimental campaign.

### 7.2.1 Underestimation of potential gradient

Let us consider first the case in which the probe is positioned in the middle of the channel at $z_c = 0$. In Fig.10 the calculated transverse potential gradient for the MHD flow at $Ha = 1000$ and $N = 1000$ is plotted as a function of $z$ at different axial locations in front of the probe whose top is positioned at $x = 0$. The potential gradient is affected by the presence of the sensor and as a result a local deficit is observed around the position $\mathrm{P}(0, 0, 0)$ of the sensor. This local reduction disappears quite rapidly by moving upstream ($x < 0$), away from the probe, where the unperturbed fully developed distribution is recovered. Nevertheless, at the axial position where in the experiments the sensing wire tips are present the disturbance is still detected and significant. The increase of $\partial\phi/\partial z$ along $z$, on both sides of the depression of the profile, indicates that the fluid in these regions accelerates to redistribute around the sensor. This local deficit and the symmetry of the potential gradient distribution

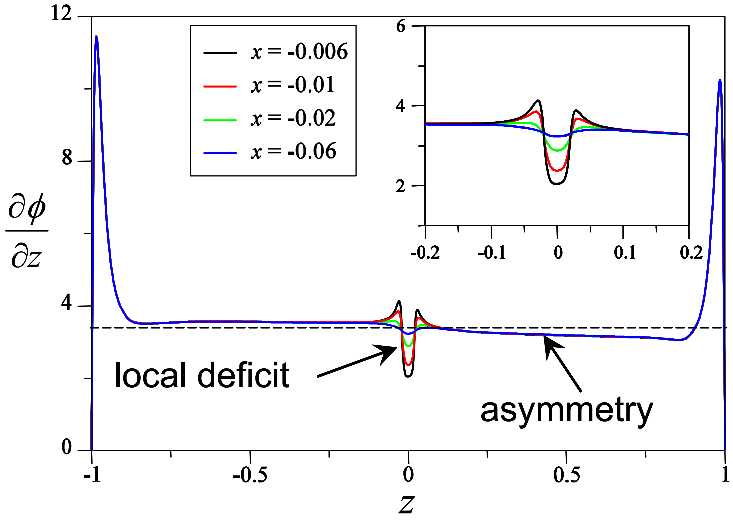

Figure 10: Transverse potential gradient plotted as a function of the coordinate $z$ at different axial positions in front of the probe, for $Ha = 1000$ and $N = 1000$. The top of the instrument is located at $(0, 0, 0)$.

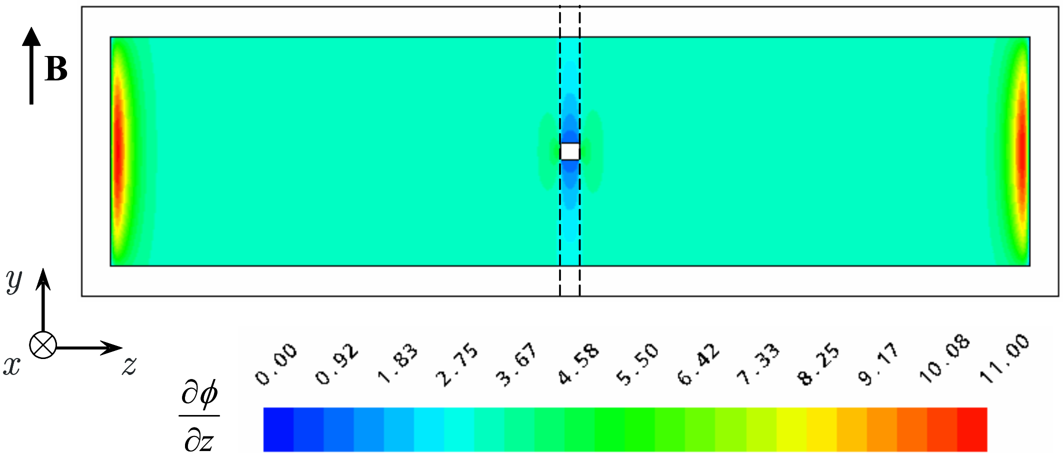

Figure 11: Contours of the transverse component of electric potential gradient $\partial\phi/\partial z$ on a cross-sectional plane passing through the probe body at $x = 0.02$, for $H\,a = 1000$, $N = 500$. The probe head is located at $z_c = 0$. Dash lines tangential to the lateral edges of the sensor mark the location of internal parallel layers.

in the case in which the metallic holder is omitted can be observed also in Fig.11 where contours of the calculated transverse potential gradient $\partial\phi/\partial z$ are displayed in a plane passing through the longitudinal body of the instrument.

This deformation of the electric potential profile is related to the perturbation of the flow caused by the probe itself. More specifically, due to the presence of the instrument, 3D current loops occur and internal layers develop along magnetic field lines tangential to the sensor, disturbing the potential gradient compared to that of a fully developed flow.

In order to clarify how the presence of the probe can affect the local flow distribution by producing non negligible currents, let's consider the curl of Ohm's law (3). In the case of a uniform magnetic field $\mathbf{B} = \hat{\mathbf{y}}$ it yields

$$\nabla \times \mathbf{j} = \boldsymbol{\nabla} \times (\mathbf{v} \times \mathbf{B}) = (\mathbf{B} \cdot \nabla)\, \mathbf{v} = \frac{\partial \mathbf{v}}{\partial y} \tag{13}$$

showing that recirculating currents are driven by velocity gradients in magnetic field direction. Around the probe variations of axial velocity $\partial v_x/\partial y$ occur in the Hartmann layers that develop along the surfaces of the sensor body where a normal component of the magnetic field is present. These gradients drive current loops as displayed in Fig.12a. In front of the sensor, where the electrodes are located, more complex recirculations are observed. They are caused by the combined contribution of the gradients $\partial v_x/\partial y$, $\partial v_y/\partial y$ of the axial and vertical components of the velocity along magnetic field direction. Figure 12b shows a projection of these current streamlines in a $yz$ plane. The occurrence of 3D phenomena around the measuring instrument is further indicated by the increase of the axial pressure gradient while approaching the probe and by the deformation of the transverse profile of electric potential.

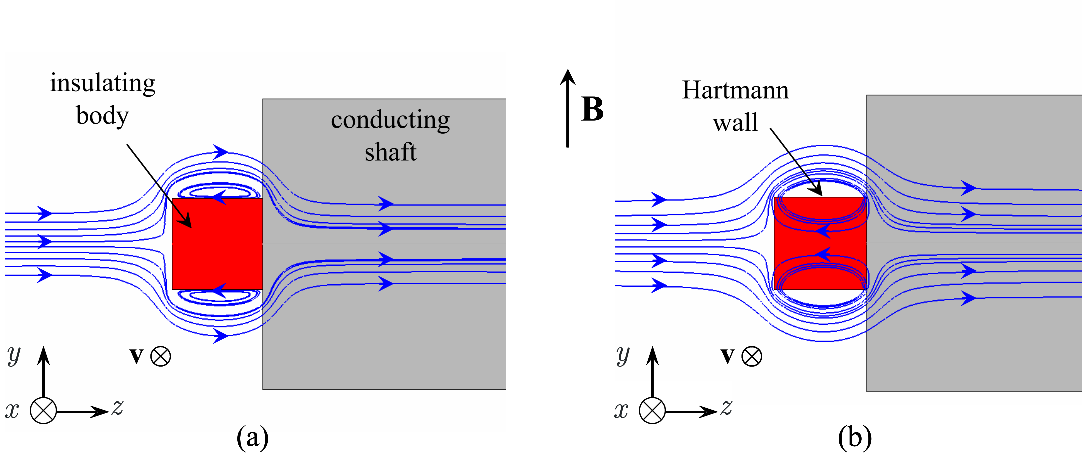

Figure 12: Projection of current streamlines on a plane (a) downstream around the sensor ($x > 0$) and (b) in front of the probe ($x < 0$) for $Ha = 1000$ and $N = 1000$. Here the sensor is located at $z_c = -0.79$, close to the side wall.

Another important flow modification related to the presence of the sensor is the occurrence of internal viscous layers. They develop along magnetic field lines tangential to the edges of the probe. Due to the small size of the instrument the internal layers, spreading from the side walls of the insulating body, tend to merge and form a unique region across which a local deficit of the transverse potential gradient occurs. This disturbance is present not only in front of the probe but also above and below it, as indicated in Fig.13a by contours of transverse potential gradient around the sensor located at $(0, 0, -0.79)$.

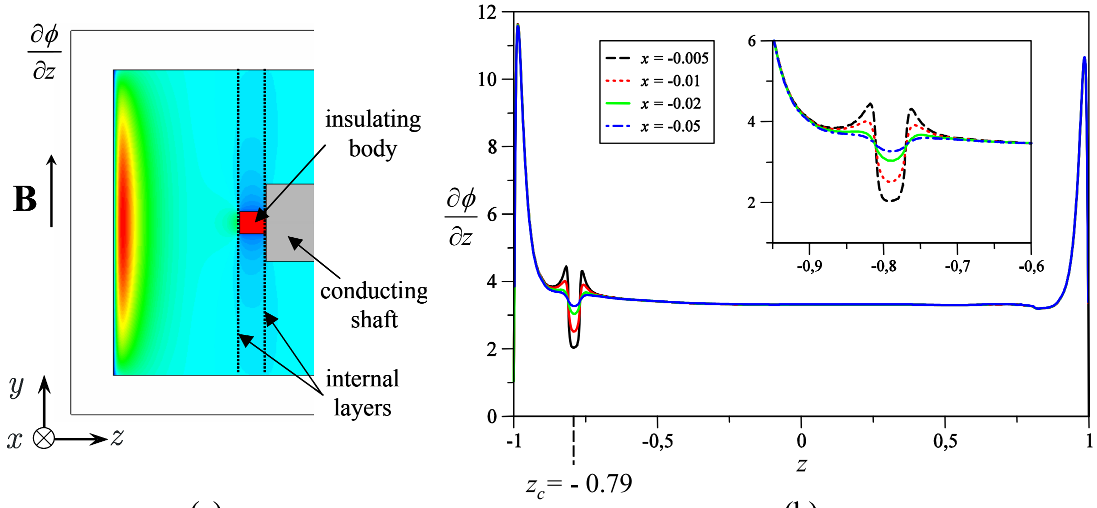

(a) (b)

Figure 13: (a) Contours of transverse potential gradient around the probe. (b) Calculated transverse potential gradient across the duct for $Ha = 1000$ and $N = 1000$ at various $x$ positions in front of the probe located at $(0, 0, -0.79)$.

The combination of the presence of recirculating currents and internal layers leads to the local reduction of the potential gradient as already shown in Fig.10 and analogously in Fig.13 for a different location of the probe.

This underestimation can be better explained by considering the sketch in Fig.14 that shows a projection of the probe on a vertical $yz$ plane and numerical results for the potential distribution. The square represents the insulating head of the instrument. Upstream at some distance from the sensor the potential in the duct has the unperturbed fully developed profile $\phi(z)$ marked by the dash line. For strong magnetic fields, i.e. for sufficiently large Hartmann numbers *Ha*, internal parallel layers develop along **B** lines tangential to both the sides of the probe, as indicated in Fig.14 by the vertical dotted lines. The flow around the instrument is strongly affected by their presence and the perturbed region may reach upstream positions where the sensing tips are located. As a result the fully developed potential profile $\phi(z)$ is disturbed as shown by $\phi'(z)$ (solid line) and the tips record a potential gradient $\Delta\phi/d$ which can be considerably smaller than that in the unperturbed flow.

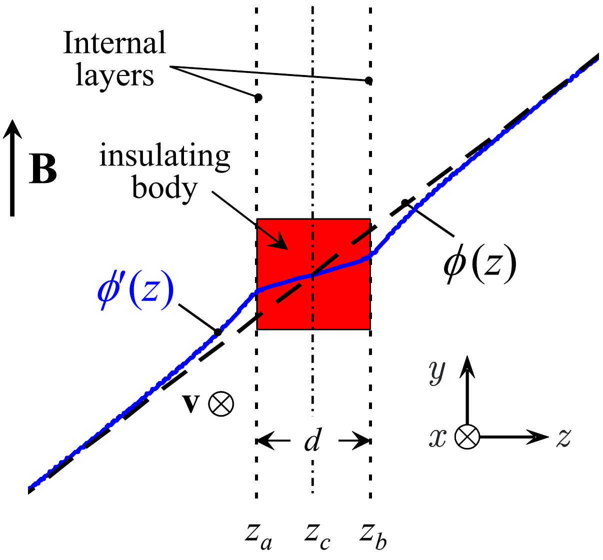

Figure 14: Calculated potential profile, for $Ha = 1000$ and $N = 1000$, immediately in front of the probe (solid line), $\phi'(z)$, and in a region of the duct where the flow is fully developed and unperturbed (dash line), $\phi(z)$. The square marks the head of the sensor whose center is positioned at $z_c$.

From Fig.14 it can be observed that the local potential $\phi'(z_a)$ at each transverse position is recorded with the same offset compared to the undisturbed one. The values $\partial\phi/\partial z$ obtained by differentiating these measured data according to (12) are not affected by this constant value. These observations give a reason for the fact that the recorded potential gradient $\Delta\phi/d$ is found to be systematically smaller than the one obtained by numerical differentiation of potential values with respect to the coordinate $z$. Therefore, a scaling of the recorded data, i.e. a suitable calibration of the sensor, is required to correct the potential difference signal including the effects of the flow perturbation caused by the measuring instrument. In the next discussion, for simplicity of notation, the prime, used to denote the perturbed potential, is omitted and the measured electric potential is simply indicated by $\phi(z)$ as in (11).

It should be noticed that the potential gradient reduction predicted numerically is smaller than the one observed experimentally. This could be due to the following differences between experiments and calculations. First, in the simulations a probe with square cross section has been chosen for simplicity instead of a circular one. Second, it has been assumed that the sensing wires are so thin that their contribution to the flow perturbation is negligible and therefore, they have been omitted in the geometric model. A full numerical approach for the present 3D geometry is already difficult because of the need of resolving all the thin boundary and internal layers that develop along duct walls and sides of the probe. Including the wires implies considering also scales that are one order of magnitude smaller than those resolved in the discussed cases.

The previous discussion aimed at explaining the systematic $N$-dependent deviation between the measured potential difference $\Delta\phi/d$ and the gradient $\partial\phi_{fit}/\partial z$ obtained by numerical differentiation of the analytical fit of experimental potential values. The next section of the report is dedicated to the analysis of the second peculiar phenomenon that characterizes the experimental data, i.e. the observed asymmetry of the measured potential gradient profiles.

### 7.2.2 Asymmetry of measured potential gradient profiles

Numerical results have been obtained by considering two geometric models. First we simulated the MHD flow in a duct containing only the longitudinal body of the probe and omitting the shaft. In a second step we increased the complexity of the geometry by including the metallic holder.

According to (10), for negligible currents, the transverse electric potential gradient may be interpreted as a measure for the axial velocity component $u$. Therefore in the following the results are described and discussed in terms of velocity. The precise relation between velocity and electric potential gradient and the degree of accuracy of expression (10) for the velocity components in a plane perpendicular to the magnetic field are discussed at the end of this section.

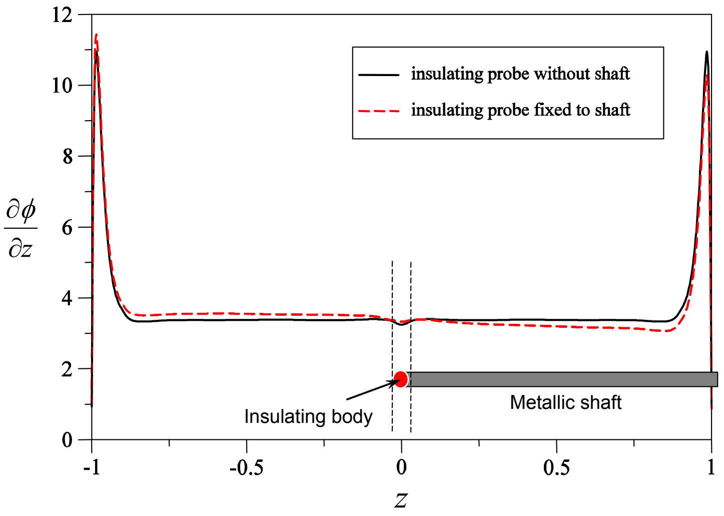

Figure 15: Calculated transverse potential gradient across the duct, on the symmetry plane ($y = 0$) at an axial coordinate corresponding to the position of the wire tips in the experiments, for $Ha = 1000$ and $N = 1000$. The solid line shows the results obtained by considering only the insulating longitudinal part of the probe at $z_c = 0$. The dash line marks the profile calculated by including the transverse metallic shaft of the instrument.

In Fig.15 the calculated transverse potential gradient is plotted along the duct width, at the symmetry plane $y = 0$. The axial position at which the profiles are given corresponds approximately to that of the sensing wire tips in the experiments ($x = -0.08$). The comparison of potential gradient profiles obtained with the two different geometric models shows that the presence of the shaft, sketched below the curves as a grey rectangle, leads to an asymmetry in the velocity distribution, as observed in the experiments. The core value and the maximum velocity of the jet in the side layer along the wall through which the probe is inserted ($z = 1$) reduce compared to those in the fully developed flow. As a consequence the velocity in the opposite side layer ($z = -1$) and in the core in the other half of the duct ($z < 0$) increases. This is due to the fact that the shaft of the instruments obstructs the flow which tends to move in the free part of the channel. Where the head of the probe is located the before described (Sect.7.2.1) local reduction of the potential gradient is clearly visible.

Current density distribution

The inclination of the velocity profile, which occurs when the shaft is included in the geometric model, can be explained also in terms of current density distribution in the duct. Three dimensional current loops and limiting current streamlines on characteristic surfaces are used in the following discussion in order to describe how the current flows around the instrument. The limiting streamlines represent a projection of the 3D current paths on a plane, therefore usually they don't indicate close loops but they are useful to identify typical and singular points produced by the considered vector field. An application of these 2D streamlines for visualization of complex velocity and current fields can be found in Mistrangelo (2005) and Bühler (2008) and in references cited there in the literature reviews.

The electrically conducting shaft of the instrument provides current paths in addition to those in the duct walls and in the thin boundary layers that develop along them. This is displayed in Fig.16 where limiting streamlines for the current vector field are plotted on a $yz$ plane, which passes through the shaft of the probe. At the side wall-fluid interface it is possible to identify a characteristic point P, which indicates that the current entering the wall splits into two parts following different paths. One portion of the current induced in the fluid moves upward in the side wall and closes through the Hartmann wall. The other one instead flows downward and along the side wall before entering the electrically conducting holder of the instrument. The line starting from the identified characteristic point and marked in the figure by the red solid line is the intersection of the channel cross-section with a surface that delimits on the upper side the area where the strongest three dimensional phenomena occur, i.e. the region in which the 3D current loops are present. In the part of the fluid domain above this line the currents follow paths similar to that indicated by the green streamline in Fig.16: the electric currents induced in the fluid flow around the shaft of the instrument and enter side and Hartmann walls or the Hartmann layer. The additional current path provided by the conducting holder leads to an increase of the total current density in the fluid, in the region around the shaft. The internal viscous layers that develop from the edges of the body of the probe, aligned with magnetic field lines, separate the cross-section distinctly in two zones with strongly different values of current density.

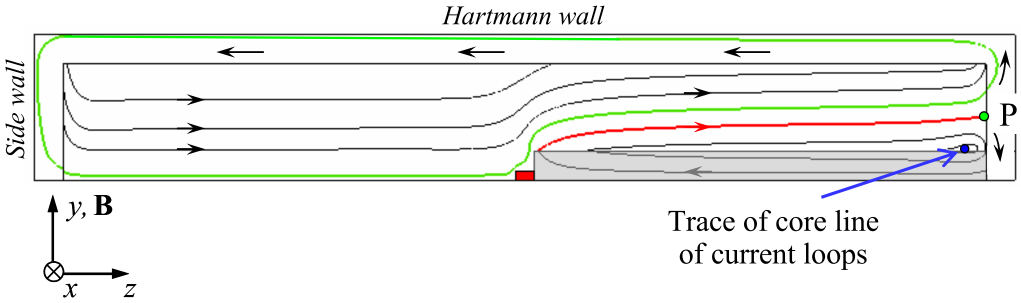

Figure 16: Limiting streamlines of electric current on a $yz$ plane passing through the shaft of the probe. Small current loops are present on the holder Hartmann wall, in the side layer. The characteristic point P indicates the location where the current entering the side wall separates into two distinct parts. Numerical results are obtained for $Ha = 1000$, $N = 500$ and probe located at $z_c = 0$.

In Fig.17 some current streamlines are depicted in front of the shaft of the instrument. They highlight the complex current distribution characterized also by 3D recirculations whose center is indicated by the presence of singular points called foci. In the region between the head and the holder of the probe electric currents induced in the fluid tend to flow along the shaft spiralling towards focus 1. Then the current moves upward and closes its path through internal parallel layers and walls. Near the side wall a vortex core line can be identified around which some current lines describe 3D paths. These current loops give rise to larger recirculations behind the holder (see also Fig.19). An overview of the topology of the current distribution in front of the shaft is illustrated in Fig.18 by means of limiting streamlines plotted on a plane passing near focus 1.

In Figs.19, 20 current streamlines are depicted behind the holder of the instrument, i.e. around the backward-facing step represented by the edge of the shaft located at $x = x_{s2}$. The current flowing around the before mentioned vortex core line gives rise to the recirculations behind the ”sudden expansion” that create the strong 3D MHD effects and electromagnetic forces that act against the fluid motion. Further downstream a second focus (focus 2) is present. At some distance from the shaft the current distribution recovers the 2D structure typical of fully developed MHD duct flow.

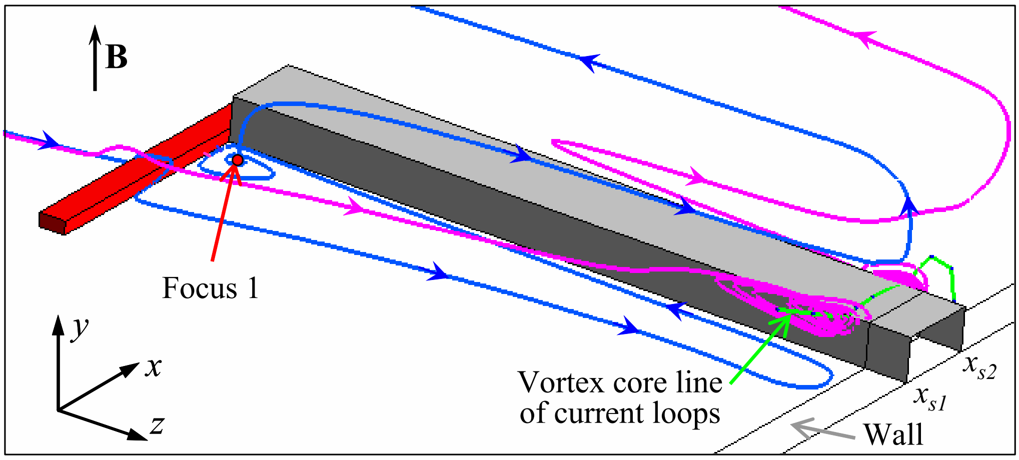
B
Focus 1
y
x
z
Vortex core line
of current loops
$x_{s2}$
$x_{s1}$
Wall

Figure 17: Characteristic current streamlines in front of the shaft of the probe. The line close to the side wall marks the center of spiralling current paths that contribute to the large 3D recirculations behind the holder. Results are obtained for $Ha = 1000$, $N = 500$, and probe at $z_c = 0$.

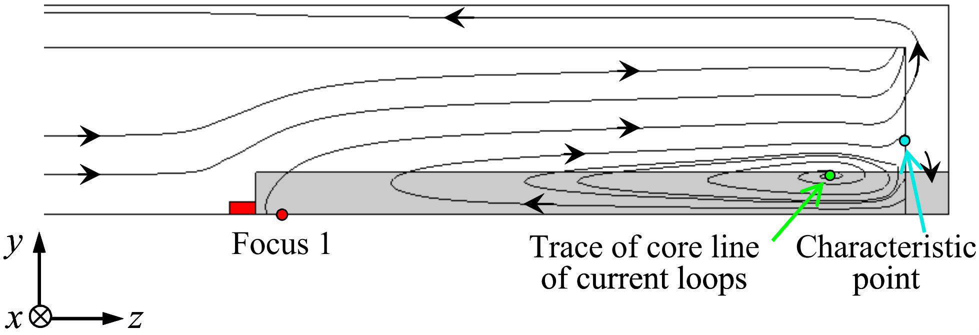
Focus 1
Trace of core line
of current loops
Characteristic
point
y
x
z

Figure 18: Trace of current streamlines on a cross-sectional plane passing in front of the shaft near Focus 1, for $Ha = 1000$, $N = 500$ and probe at $z_c = 0$.

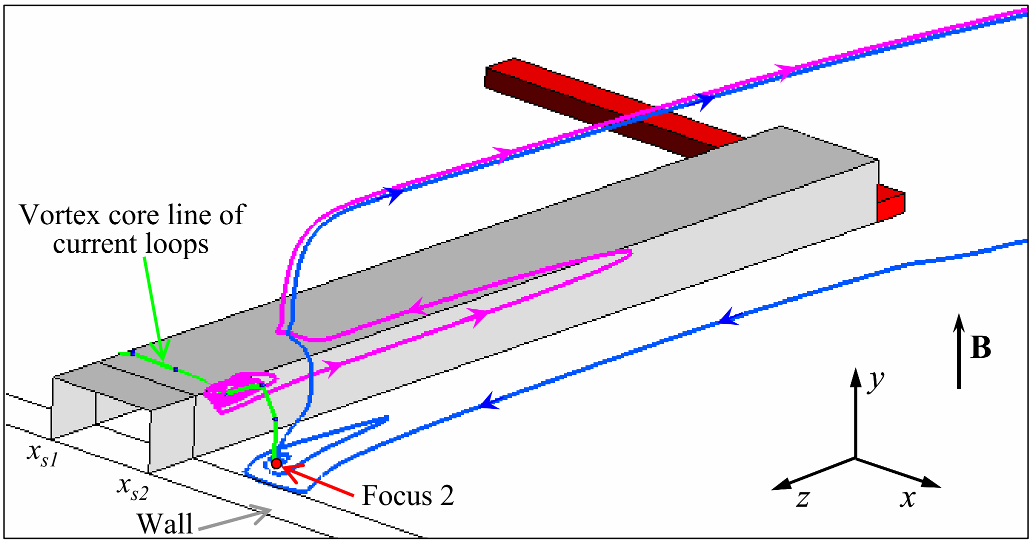
Vortex core line of current loops
B
y
z
x
$x_{s1}$
$x_{s2}$
Wall
Focus 2

Figure 19: Characteristic current streamlines behind the shaft of the probe. The line close to the side wall marks the center of vortical current loops that contribute to the large depicted 3D recirculations. Results are obtained for $Ha = 1000$, $N = 500$, and probe located at $z_c = 0$.

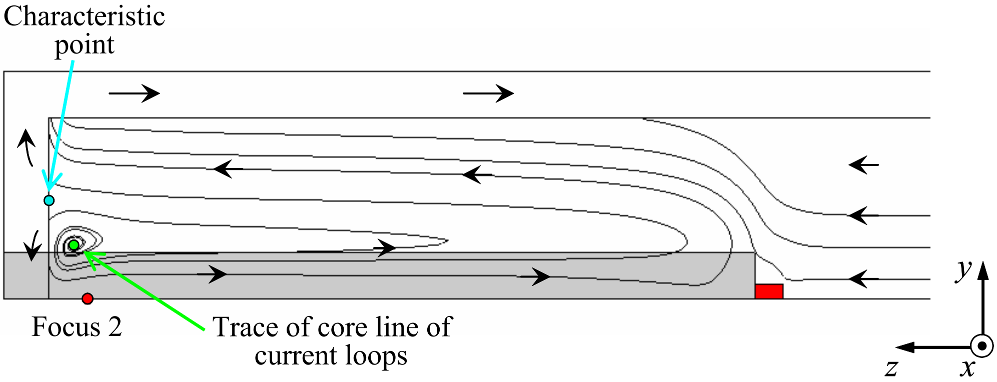
Characteristic point
Focus 2
Trace of core line of current loops
y
z
x

Figure 20: Trace of current streamlines on a cross-sectional plane passing near focus 2. Results are obtained for $Ha = 1000$, $N = 500$, and probe located at $z_c = 0$.

Internal parallel layers

Internal layers develop along all the surfaces that are aligned with the magnetic field. They spread into the fluid also from the edges of the shaft of the probe. Their formation is due to the combination of different factors like the discontinuity in the wall conductivity, represented by the holder, and the redistribution of the flow around this obstacle.

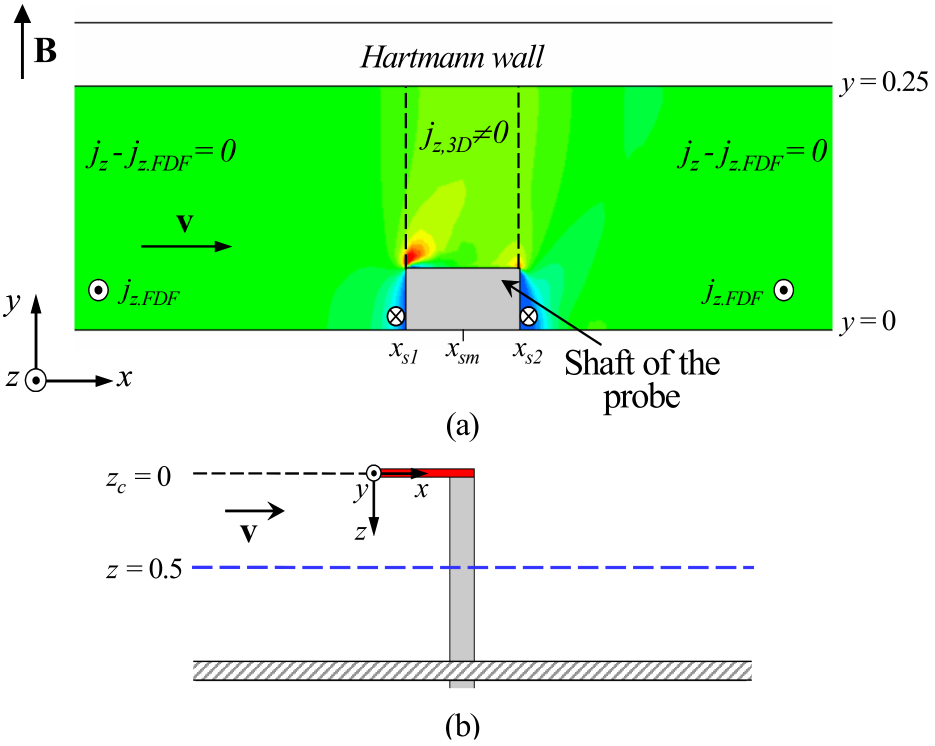

Figure 21: Contours of the difference between the transverse current component $j_z$ and its constant value $j_{z,FDF} = -\partial p/\partial x \simeq 0.41$ in the fully developed region, for $Ha = 1000$, $N = 500$ and probe located at $z_c = 0$. The considered plane is at $z = 0.5$, i.e. it passes through the middle of the shaft as marked by the blue line in sketch (b). Blue color indicates minimum negative values and red the maximum positive transverse current. Dash lines mark the location of parallel layers.

In Fig.21a the contours of the perturbation of current due to the probe, $j_z - j_{z,FDF}$, are depicted on a $xy$ plane. Here $j_z$ and $j_{z,FDF}$ represent the transverse current density component in presence and in absence of the instrument, respectively, i.e. $j_{z,FDF}$ gives the current density of a fully developed flow. In the following discussion the quantity $j_z - j_{z,FDF}$ will be referred to as $j_{z,3D}$ since it is related to the 3D MHD phenomena caused by the flow perturbations introduced in the fluid by the instrument. The considered plane is located at $z = 0.5$, namely it crosses the shaft through its middle point. The trace of this plane is marked by the blue dash line in

Fig.21b. In Fig.21a the blue color corresponds to negative values of $j_{z,3D}$, i.e. the current is moving in direction opposite to that of the fully developed flow. The red instead marks the largest positive transverse current density. The area of increased current density extends along the entire height of the duct. This is due to the fact that the internal shear layers develop along **B**-lines from the probe shaft towards the duct Hartmann wall. The presence of these layers and the 3D current loops represent an obstacle for the fluid that tries to bypass this region by moving towards the other free half part of the duct ($z < 0$). These observations explain the above mentioned asymmetry of the transverse potential gradient profile and the smaller values in the portion of the channel containing the holder of the instrument (see Fig.15). Figure 21a shows also that the internal parallel layers separate the fluid domain in three different regions. More specifically, there are two cores where, upstream and downstream, at some distance from the shaft, fully developed conditions are observed and a zone between the two layers in which strong flow perturbations and 3D current loops occur.

The axial extent of the perturbed area is clearly expressed by the streamwise pressure gradient $\partial p/\partial x$ that takes non-constant values both in front and behind the instrument.

In Fig.22 the pressure is plotted as a function of the axial coordinate, along a line located at $z = 0.5$, passing above the shaft of the instrument. It can be observed that the pressure distribution resembles that in a duct formed by a step located at $x = x_{s1}$ and a backward-facing step at $x = x_{s2}$. In other words the geometry consists of an asymmetric contraction followed by a single-side sudden expansion. The dotted lines show the constant pressure gradient ($\partial p/\partial x \simeq -0.41$) upstream and downstream, sufficiently far from the instrument, where fully developed flow conditions are established. By approaching the holder of the probe the pressure drops rapidly and the magnitude of the axial pressure gradient increases compared to that in the fully developed flow. Immediately in front of the backward-facing step, the magnitude of the pressure gradient reduces and at the sudden expansion ($x \simeq x_{s2}$) it changes sign. Behind the step, for $x > x_{s2}$, a partial recovery of pressure occurs (Bühler (2008)) as displayed in Fig.22a.

By considering the axial distribution of the pressure at different transverse positions, as depicted in Fig.23, it can be observed that also on the other side of the probe, i.e. for $z < 0$, the pressure gradient $\partial p/\partial x$ differs from that in a fully developed MHD flow when moving closer to the axial location of the shaft of the instrument ($x = x_{s1}$). This perturbation disappears by moving towards the side wall at $z = -1$. The disturbance in the pressure distribution occurs over an axial distance smaller than one characteristic length symmetrically with respect to the location of the shaft of the probe as displayed in Fig.23. Upstream and downstream all the curves merge, indicating that the computational domain is long enough to ensure that fully developed conditions are established at some distance from the probe.

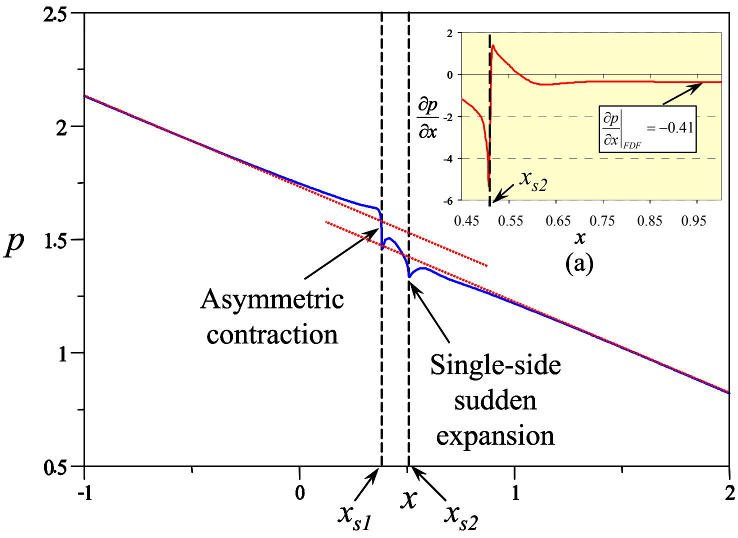

Figure 22: Pressure as a function of the $x$- coordinate and (a) axial pressure gradient across the "sudden expansion" located at $x = x_{s2}$, plotted along the line at $z = 0.5$, $y = 0.065$, passing above the metallic shaft. Results are given for $Ha = 1000$, $N = 500$ and probe at $z_c = 0$.

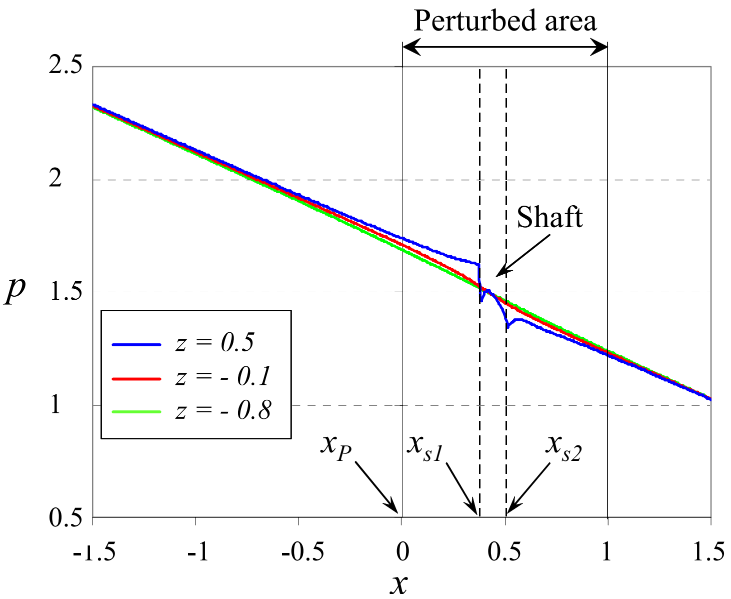

Figure 23: Axial pressure distribution along lines at $y = 0.065$, above the shaft, for various transverse positions, for $Ha = 1000$, $N = 500$ and probe at $z_c = 0$. The region where $z < 0$ is the one where the shaft is not present. The points $x_P$, $x_{s1}$ and $x_{s2}$ indicate the axial location of the top of the probe head and of the two sides of the shaft, respectively.

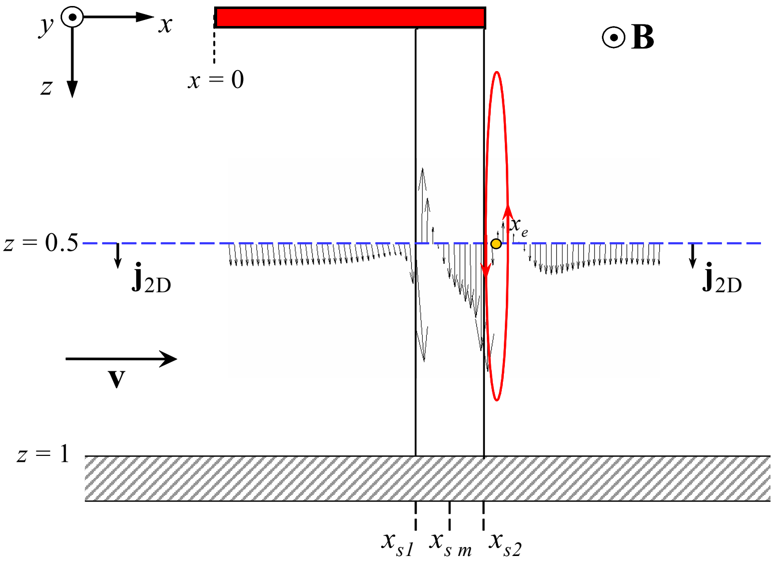

Figure 24: Calculated current density distribution on the plane $y = 0.065$ explaining the 3D MHD effects that occur around the shaft of the probe. The points having axial coordinates $x_{s1}$, $x_{s,m}$ and $x_{s2}$ mark the beginning of the shaft, the middle point and the end, respectively. The point $x_e$ is the location where $j_z$ changes sign behind the holder.

The sudden variation of the axial pressure gradient that occurs when the flow passes above the backward-facing step, can be explained by considering the current distribution in this region, as depicted in Fig.24. Upstream and downstream, far from the instrument, the flow is fully developed and 2D currents $\mathbf{j}_{2D}$ flow in the positive transverse direction. For $x > x_{sm}$, namely in front of the backward-facing step, near the side wall ($z = 1$) the combination of the effects due to the enlargement of the cross section, the discontinuity of the wall conductivity and the formation of Hartmann layers on the holder top surface gives rise to a non uniform axial potential gradient and to recirculating 3D current loops in the region around the shaft.

Figure 25 shows the transverse component of the current density along a line at $z = 0.5$, $y = 0.065$ above the shaft. The positive $z$-component of the current yields a Lorentz force that tends to block the flow, and instead the negative one results in electromagnetic forces that accelerate the fluid. This results in a pressure recovery for $x > x_{s2}$ as already observed. The area where the positive transverse current rises strongly correspond also to the location of the most intense gradients of the velocity. The point where $j_z$ vanishes can be regarded as a possible indication for the thickness of the internal layers that develop from the shaft towards the channel Hartmann wall (see Mistrangelo (2005)).

The redistribution of the flow behind the holder of the instrument can be seen also by considering the variation of the vertical component of the velocity on a $xy$ plane. Figure 26 displays the contours of vertical velocity $v$ on the plane $z = 0.5$ showing the strong downward flow behind the probe in the internal layer at $x = x_{s2}$.

Considering the velocity field around the instrument, other analogies with the

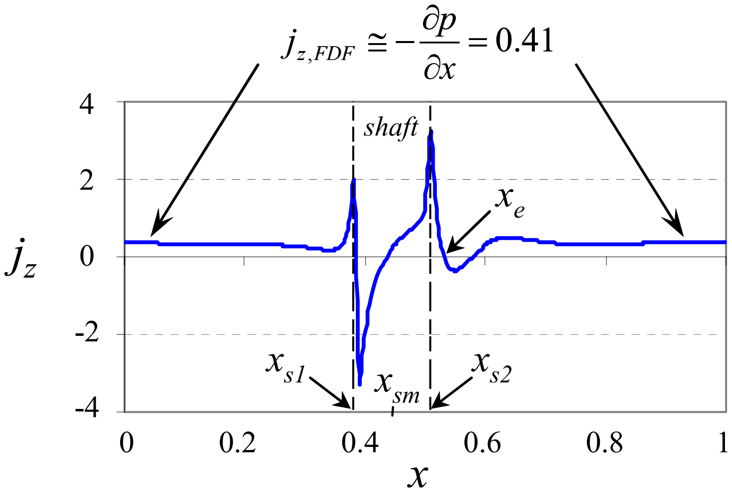

Figure 25: Transverse current density as a function of the axial coordinate $x$ for $Ha = 1000$, $N = 500$, probe at $z_c = 0$. The line along which the profile is plotted is positioned at $z = 0.5$, above the metallic holder of the instrument ($y = 0.066$).

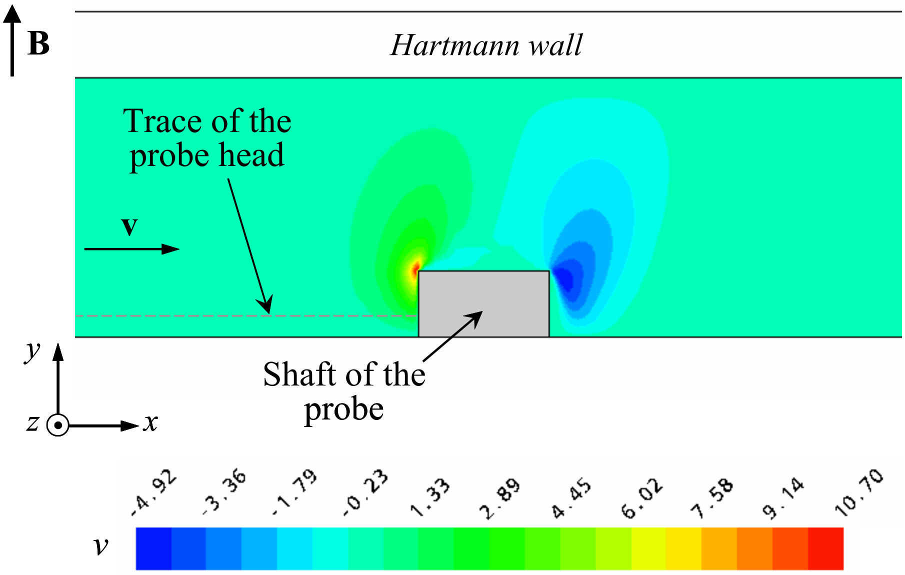

Figure 26: Contour plots of the vertical component $v$ of the velocity on the plane $z = 0.5$ passing through the shaft of the instrument. For clarity, even if not visible, the trace of the insulating body of the probe is marked by a grey dash line. Results are obtained for $Ha = 1000$, $N = 500$, probe at $z_c = 0$.

MHD flow in sudden expansions as available in the literature can be found. An accurate description of MHD flows in a symmetric sudden expansion with high aspect ratio can be found in Mistrangelo (2005) or Bühler (2008).

As a further example, in Fig.27 the contours for the transverse velocity are depicted on a plane close to the side wall ($z = 0.98$). The blue zone indicates a region of negative transverse velocity, i.e. the fluid moves to the center of the duct inside the internal **B** field-parallel layer that develops at the sudden expansion. Behind the backward-facing step the flow detaches from the wall and a recirculation can be observed whose center is marked by the focus F (Figs.27a,b).

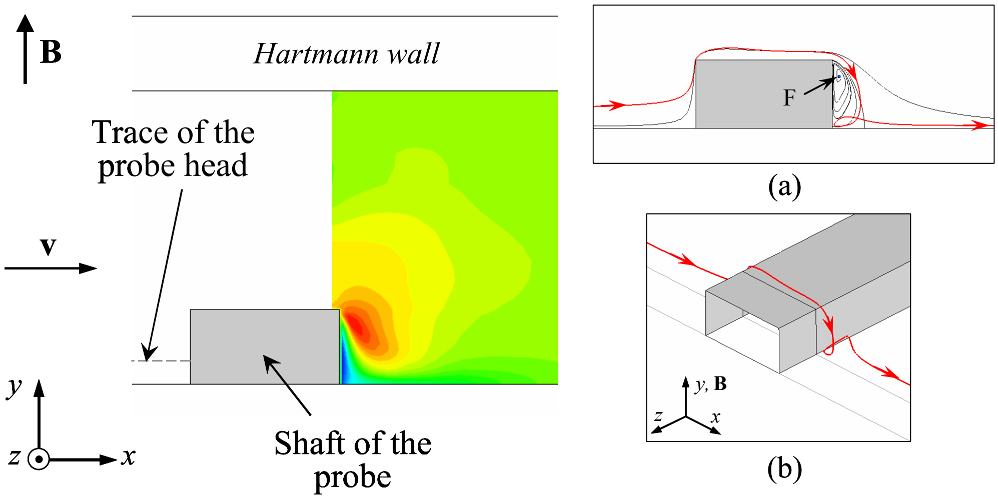

Figure 27: Contour plots of the transverse velocity $w$ on a plane near the side wall of the duct ($z = 0.98$), for $Ha = 1000$, $N = 500$ and probe at $z_c = 0$. (a), (b) Flow paths around the shaft of the probe. The point F marks the focus of the recirculation due to the detachment of the flow. behind the backward facing step.

During the experimental campaign questions arose about the need of insulating the metallic holder on which the head of the probe is fixed. For this reason preliminary calculations have been performed to understand the effects on the flow distribution of the electrical properties of the shaft.

In Fig.28 numerical results for $Ha = 1000$ and $N = 500$ show the transverse potential gradient across the channel width. Profiles have been obtained by considering an electrically conducting (red dash line) or insulating (blue solid line) shaft and by simulating only the longitudinal body of the instrument without the shaft (solid black line). The insulation of the holder reduces slightly the asymmetry of the potential gradient profile but it seems not to affect the local deficit that occurs at the top of the instrument where the sensing wires are located. Even if further studies are foreseen to better define the influence of the electrical properties of the shaft on the flow distribution, from a first analysis it seems that the conductivity of the holder

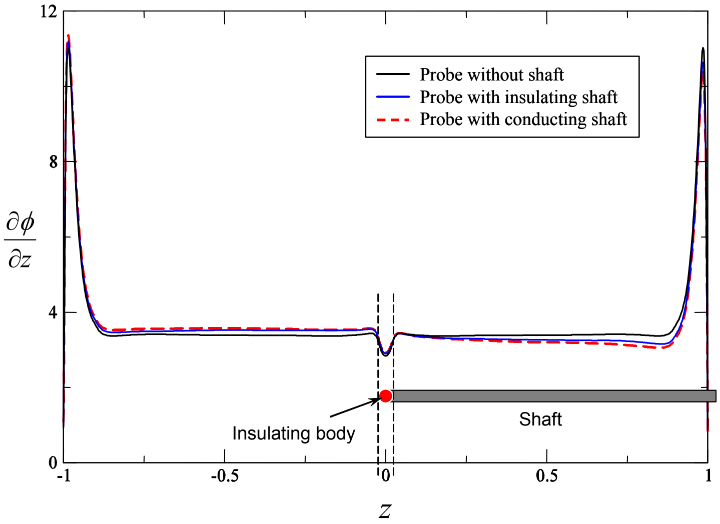

Figure 28: Calculated transverse potential gradient across the duct, on the symmetry plane ($y = 0$) at an axial coordinate ($x \simeq 0$) immediately in front of the probe head, for $Ha = 1000$ and $N = 500$. Three different cases are compared: 1) only the insulating longitudinal part of the probe at $z_c = 0$ is considered (solid black line), 2) the transverse shaft (grey rectangle shown below the curves) is insulating (solid blue line), 3) the shaft is electrically conducting (dash red line).

does not contribute significantly to the observed local reduction of the recorded potential gradient. This is also confirmed by the results discussed in Sect.7.2.1 that highlight the fact that reasons for this underestimation of potential gradient can be found in the occurrence of internal layers and recirculating currents around the top of the probe. These phenomena are not modified by the electrical properties of the shaft.

### 7.2.3 Extent of perturbed region around the probe

In order to estimate the longitudinal extend of the region perturbed by the potential sensor, let us consider the results for the case in which the probe is located close to the side wall at $z_c = -0.79$. In Fig.29a the transverse potential gradient is plotted in axial direction along a line passing through the probe ($z = -0.79$) and along lines in the two side layers at $z = \pm 0.985$. A sketch of the probe inside the channel and the considered lines are displayed in Fig.29b. The profile of the potential gradient in front of the probe (blue dash line) indicates that strong disturbances are confined to upstream distances of about three times the size of the probe. Instead in the side layer opposite to the entrance of the instrument (dot-dash line at $z = -0.985$) the perturbation extends for about three characteristic lengths ($-1 < x < 2$). Here the potential gradient distribution shows that, when moving near the axial position

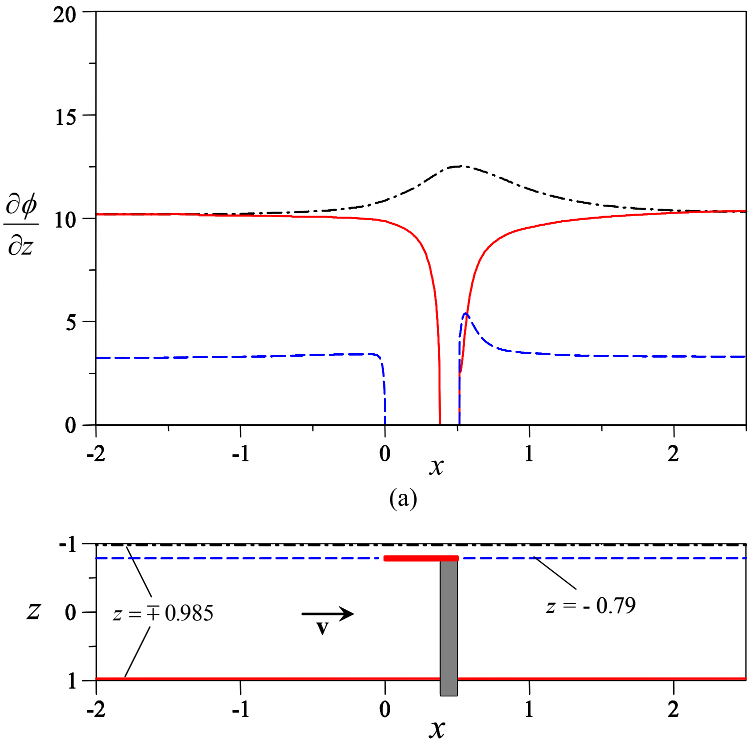

(a)

(b)

Figure 29: (a) Transverse potential gradient as a function of the axial coordinate $x$ along a line passing through the probe ($z = -0.79$), and lines in side layers ($z = \pm 0.985$). Results are obtained for $Ha = 1000$ and $N = 1000$. (b) Schematic representation of the probe and position of considered lines.

of the probe, the velocity of the jet increases compared to that in the inlet fully developed flow. The rise is quite evident in this case since the probe is very close to the side wall at $z = -1$ and therefore the shaft crosses large part of the duct cross-section obstructing the stream. The results displayed in Fig.30 refer instead to the case in which the sensor is at $z = 0$. The increase of the velocity in the side layer ($z = -0.985$) is much smaller than in the previous case since only half of the channel is crossed by the holder. These outcomes confirm some of the arguments discussed in Sect.7.2.2, used to explain the asymmetry of the transverse potential gradient profile in the duct.

By comparing results for a constant Hartmann number and various interaction parameters, it can be noted that when reducing $N$ the undisturbed velocity distribution is recovered further downstream, due to the stronger inertia effects. Moreover, disturbances induced by the probe propagate upstream within a shorter distance.

As part of the experimental campaign measurements have been taken also in the square duct of the expanding test section (Fig.1). The evaluation of these data shows that the perturbations caused by the body of the probe are less pronounced than in the slender channel. This is due to the different relative size of the probe compared

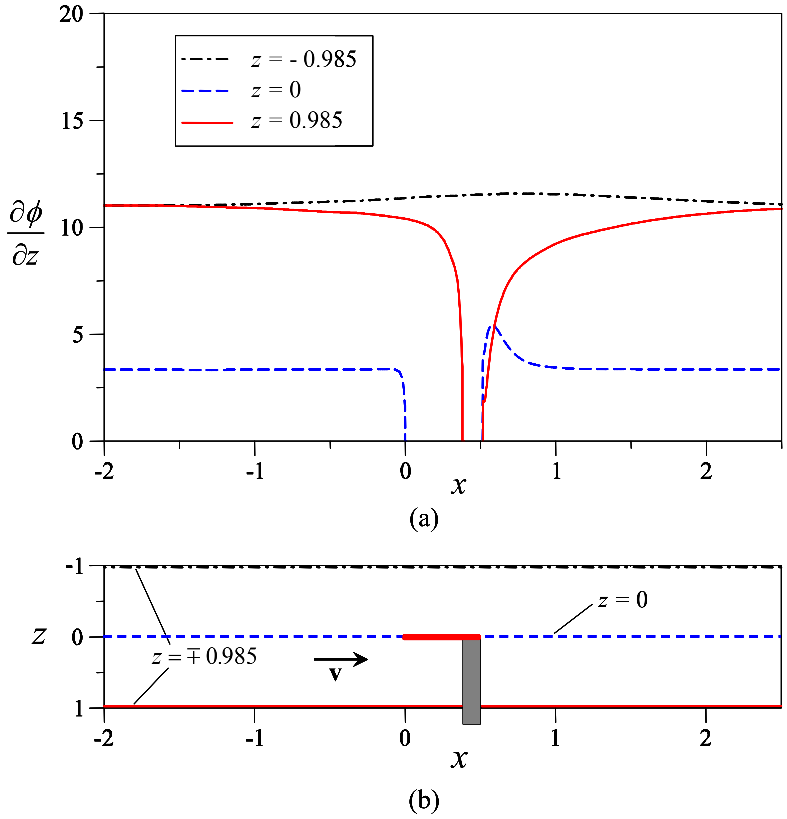

Figure 30: (a) Transverse potential gradient as a function of the axial coordinate $x$ along a line passing through the probe ($z = 0$), and lines in side layers ($z = \pm 0.985$). Results for $Ha = 1000$ and $N = 500$. (b) Schematic representation of the probe and considered lines.

to the Hartmann lengths in the two ducts. With respect to that the instrument represents a much larger obstacle for the flow in the flat inlet channel than in the outlet one.

## 7.3 Calibration of experimental data

The previous discussion and the detailed evaluation of the experimental results for constant Hartmann numbers highlighted the dependence of the measured potential difference distribution on the interaction parameter. This influence of inertial forces has been observed for all the values of the magnetic field that have been investigated during the measuring campaign, even if for sufficiently high Hartmann numbers the strong electromagnetic forces tend to dominate reducing the systematic $N$-dependent deviation of the data.

Figure 31a displays experimental values of the potential gradient $\Delta\phi/d$ recorded by the probe along the duct width for various interaction parameters $N$ and a con-

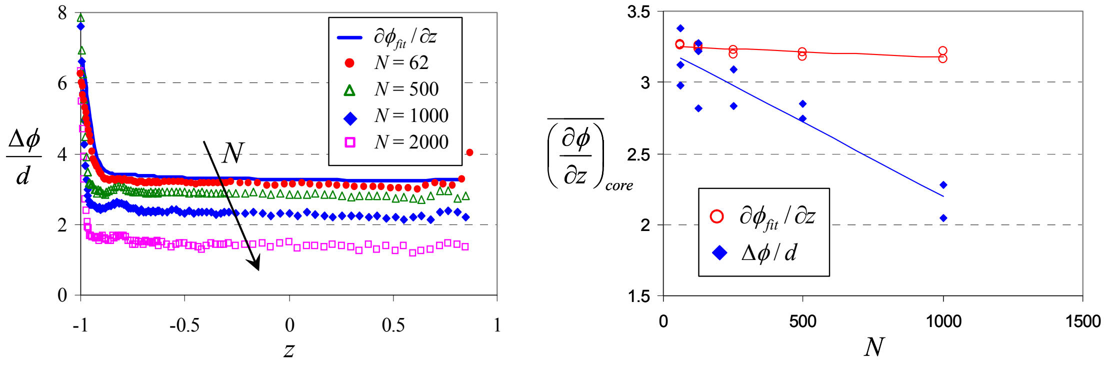

(a) (b)

Figure 31: (a) Measured potential gradient $\Delta\phi/d$ for various $N$ compared with $\partial\phi_{fit}/\partial z$ for $N = 62$. (b) Average value in the duct core of transverse potential gradient obtained by differentiation of the fit of measured potential with respect to $z$, $\partial\phi_{fit}/\partial z$, and by direct measurement, $\Delta\phi/d$, as a function of $N$, for $Ha = 1000$.

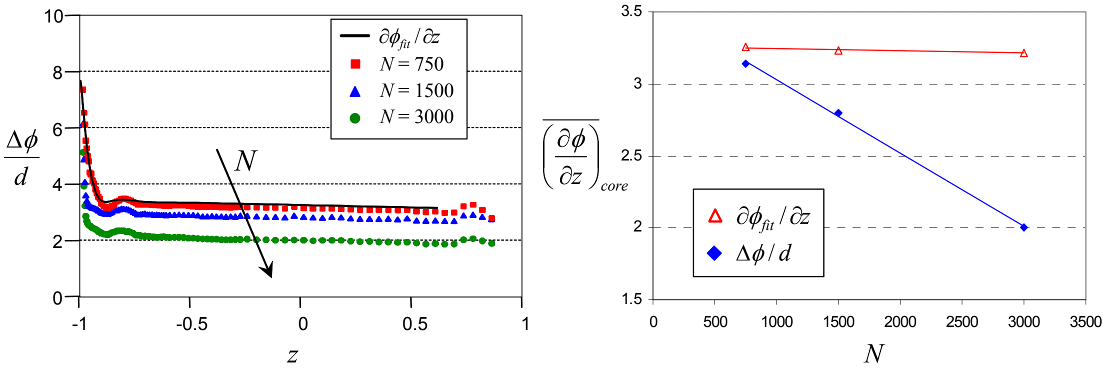

(a) (b)

Figure 32: (a) Measured potential gradient $\Delta\phi/d$ for various $N$ compared with $\partial\phi_{fit}/\partial z$ for $N = 750$. (b) Average value in the duct core of transverse potential gradient obtained by differentiation of the fit of measured potential with respect to $z$, $\partial\phi_{fit}/\partial z$, and by direct measurement, $\Delta\phi/d$, as a function of $N$, for $Ha = 3000$.

stant Hartmann number $Ha = 1000$. They are compared with the potential gradient profile $\partial\phi_{fit}/\partial z$ determined by differentiation with respect to $z$ of the measured local potential $\phi(z)$ at $N = 62$. It is observed that by decreasing $N$, the deviation between the two quantities $\Delta\phi/d$ and $\partial\phi_{fit}/\partial z$ reduces, i.e. the local depression of the potential gradient at the measuring point becomes smaller. This can be caused by the fact that for higher velocities the stronger inertia forces shorten the axial size of the perturbed area, shifting the disturbances further downstream behind the location of the measuring tips, so that the sensing wire are placed out of the strongly disturbed region. Figure 32a shows similar outcomes for the potential differences recorded at $Ha = 3000$, for various interaction parameters $N$. The measured approximate potential profiles $\Delta\phi/d$ are compared with $\partial\phi_{fit}/\partial z$ at $N = 750$.

Profiles of transverse potential gradient $\partial\phi/\partial z$ obtained by numerical and asymptotic methods for fully developed MHD duct flows have been compared with the experimental data for various Hartmann numbers and interaction parameters. The results showed a very good agreement. This confirms the reliability of the measuring technique employed for recording. Since in the core $\partial\phi_{fit}/\partial z$ does not change with $N$, as described in Sect.7.1.1, this quantity has been chosen as a reference. A scaling procedure has been defined such that the experimental data for potential gradient $\Delta\phi/d$ match those from differentiation of the potential values $\partial\phi_{fit}/\partial z$.

In order to determine a suitable scaling factor for the experimental data, let us consider the average value in the duct core of the differentiated fit of the recorded potential , $\overline{\partial\phi_{fit}/\partial z}_{core}$, and of the measured potential gradient, $\overline{\Delta\phi/d}_{core}$.

This is described in Figs.31b and 32b where these quantities are plotted as a function of $N$ for $Ha = 1000$ and $Ha = 3000$, respectively. As expected, the derivative $\overline{\partial\phi_{fit}/\partial z}_{core}$ (diamonds) remains almost constant while $\overline{\Delta\phi/d}_{core}$ (triangles) shows a strong $N$-dependence. The ratio of the two curves has been used as scaling factor $A$. This latter one accounts for the effects of internal layers and 3D circulating currents caused by the instrument. After such calibration, whose result is shown in Fig.33 for $Ha = 1000$ and Fig.34 for $Ha = 3000$, the potential differences measured by the probe can be used to get reliable data for transverse potential gradients. We can notice that the corrected potential gradient distribution in the side layers is still affected by inertia. As mentioned in Sect.7.1.1 this has its origin in instabilities occurring in the side layers at a certain Reynolds number. However, the time-dependent behavior is observed only near the side walls while the core flow remains completely laminar and doesn't depend on the interaction parameter.

Further considerations are required in order to use the scaled experimental potential gradient to represent the velocity in the duct. As shown by (9) the determination of the velocity components $\mathbf{v}_\perp$ perpendicular to the applied magnetic field requires the knowledge of the current density. In the duct core, where the velocity distribution is uniform and the main balance of forces is established between pressure and Lorentz forces, the current density components can be expressed as $j_z = -\partial p/\partial x$ and $j_x = \partial p/\partial z$. In the side layers, when the walls are well conducting, the same value for current density is still approximately valid. For that reason current density can be estimated from pressure drop measurements (e.g. $\partial p/\partial x = -0.406$ for the present

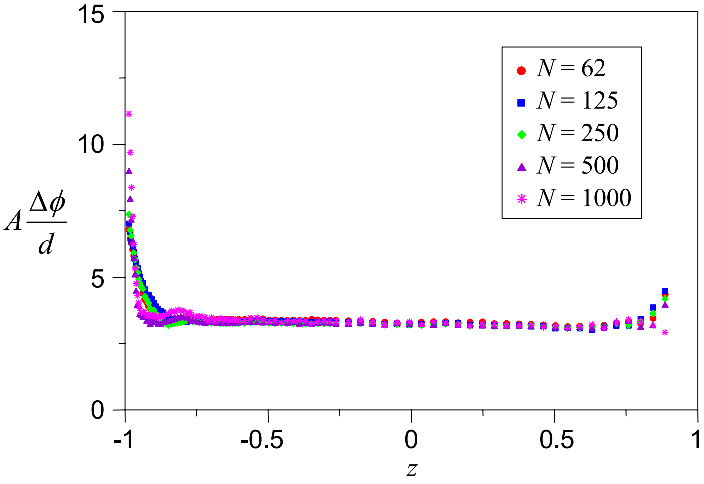

Figure 33: Scaled potential gradient $\partial\phi/\partial z = A\,\Delta\phi/d$ measured with a potential difference probe for different interaction parameters $N$ and $Ha = 1000$.

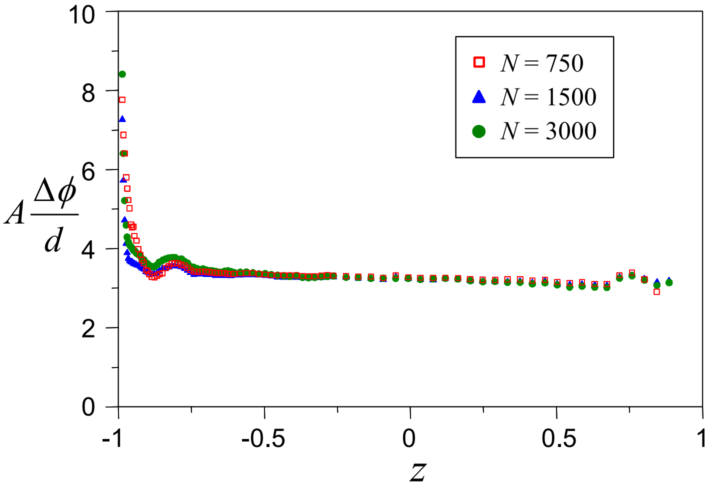

Figure 34: Scaled potential gradient $\partial\phi/\partial z = A\,\Delta\phi/d$ measured with a potential difference probe for different interaction parameters $N$ and $Ha = 3000$.

experiment) and introduced in (9) to obtain a better approximation of velocity from the experimental data for potential gradient.

Considering the additional contribution given by the current density, we may determine finally a good estimate of the velocity profile $u(z)$.

In Fig.35 the calculated axial velocity $u$ is plotted along the $z$ coordinate and is compared with the potential gradient $\partial\phi/\partial z$ and the transverse component of the current density $j_z$, knowing that $u = \partial\phi/\partial z + j_z$ (9). The results are obtained for $Ha = 1000$ and $N = 1000$, when the probe is in the center of the channel. It is interesting to observe that in the core the value of the transverse potential gradient is about 11% lower than the one of the axial velocity $u$. It has been verified that, by changing the interaction parameter, this reduction is always of the same order.

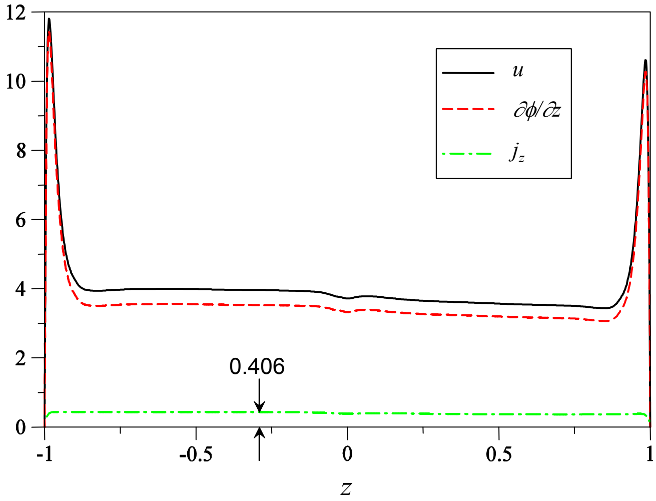

Figure 35: Comparison of calculated axial velocity $u$, potential gradient $\partial\phi/\partial z$ and transverse current component $j_z$ for $Ha = 1000$, $N = 1000$ with a probe positioned at $z_c = 0$.

# 8 Conclusions

Measurements of values and gradients of electric potential for MHD flows in electrically conducting rectangular channels have been carried out by using an electromagnetic velocity instrument. The present investigation of the experimental data is based mainly on the comparison between the gradient $\partial\phi_{fit}/\partial z$ of a smooth fit of the recorded local potential and the approximate value $\Delta\phi/d$ directly measured between two tips of the used potential difference probe. The systematic analysis of experimental data shows a discrepancy between $\partial\phi_{fit}/\partial z$ and $\Delta\phi/d$. While for a constant Hartmann number the former one remains unchanged in the core and in very good accordance with theoretical predictions for all the values of $N$ as expected for MHD fully developed duct flow, values of measured potential gradients $\Delta\phi/d$ are always smaller than $\partial\phi_{fit}/\partial z$ and show a distinct dependence on the interaction parameter $N$. The deviation from $\partial\phi_{fit}/\partial z$ increases monotonically with $N$. Nevertheless, qualitatively the signal profiles $\Delta\phi/d$ agree well with $\partial\phi_{fit}/\partial z$. This confirms the validity of the employed measuring technique and the question arises about the reason for the $N$-dependent deviation and the need of careful calibration of the experimental results is envisaged. Moreover, experimental observations reveal that the recorded potential profile is "inclined" towards the side wall through which the probe is inserted.

A numerical study of 3D MHD flows around the probe has been performed in order to investigate the reasons for the observed discrepancies of the measured quantities. Results are compared with experiments to estimate the influence of the instrument on the flow pattern and to determine the degree of perturbation that the probe imposes on the flow. The computational data are used to support a proper physical interpretation of the potential difference measurements and to determine, when required, a suitable scaling procedure that allows using the recorded potential gradient as a measure for the velocity components in a plane perpendicular to the imposed magnetic field. The aim of the present work is to highlight the difficulties that can arise when measuring potential gradients with a two-electrode probe and to give an indication how these results can be improved by proper calibration, at least in the stationary regime.

Calculations indicate as possible causes of the systematic $N$-dependent underestimation of the measured potential gradient the formation around the sensor of internal viscous layers and circulating currents produced by the instrument itself. They disturb the flow and perturb the potential distribution compared to the one of a fully developed MHD duct flow. The 3D current loops are driven by velocity gradients along magnetic field direction. These velocity variations occur both in the Hartmann layers at probe surfaces where the magnetic field has a normal component and in front of the sensor owing to the flow redistribution around it. The viscous parallel layers spread across the fluid from the edges of the instrument along magnetic field lines. As a result the perturbations propagate through the entire height of the duct.

The asymmetry of the potential profile is caused instead by the presence of the holder of the instrument that obstructs the flow. Furthermore, large 3D current loops appear in front and behind the shaft that create an electrical blockage of the stream. As a consequence, the fluid tends to flow in the free part of the duct where the shaft is not present. This produces the observed increase of the velocity in that part of the channel.

A calibration procedure has been defined from the comparison of the gradient obtained by differentiation of the measured potential $\partial\phi_{fit}/\partial z$ and the one $\Delta\phi/d$ directly recorded. Since the core value of the gradient $\partial\phi_{fit}/\partial z$ does not depend on $N$, this quantity is assumed as a reference to scale the measured potential differences. Such a scaling permits getting reliable information about the velocity distribution in the channel using the recorded approximate potential gradient. The scaled results are in agreement with numerical and analytical solutions for fully developed MHD duct flows and consistent for all Hartmann numbers $Ha$ and interaction parameters $N$ used during the experimental campaign.

The comparison between numerical results and experiments highlights the fact that the only effect of the presence of the probe on the potential gradient $\partial\phi_{fit}/\partial z$ is the asymmetry of this profile. Therefore, we conclude that reliable measurements of potential gradients can be performed by using a one-electrode movable probe as employed for instance by Kirillov, Reed, Barleon and Miyazaki (1995). In this way the local potential is recorded as the difference between the value at the measuring tip and the one at a reference ground electrode on a wall of the duct. This would also permit minimizing the size of the probe and reducing further the perturbation that the instrument causes. The potential gradient is then obtained by differentiating the recorded potential profile or a smooth analytical fit of the measured values with respect to the transverse coordinate and no calibration is required. Nevertheless, this procedure is valid only for stationary flows or for time averaged signals. Instead in order to measure the intensity of time dependent velocity fluctuations it is necessary to use a probe with more than one electrode. In this case the suggested calibration procedure has to be applied for obtaining correct values of mean profiles of potential gradient. For judging about the influence of the probe on time-dependent signals one should perform 3D numerical simulations of turbulent flows around the probe. This would allow finding out if the proposed calibration applies also to this kind of flows. This problem is beyond our present numerical capabilities and the scope of this study.

The discussed scaling procedure has been determined by considering only the value of the potential gradient in the duct core. A further improvement of the calibration could be achieved by using a local factor that accounts for the particular potential gradient profile, i.e. the local velocity in the channel.

Calculations show that, even in the case of fully developed MHD flow, the proper determination of velocity components by using the measured potential gradients requires the knowledge of the current density in the analyzed domain. In particular, the scaled measured potential gradient can be used to properly represent the velocity field in the duct by considering current density components defined in terms of pressure gradients.

# References

Andreev, O., Kolesnikov, Y. and Thess, A.: 2007, Experimental study of liquid metal channel flow under the influence of a non-uniform magnetic field, *Physics of Fluids* **19**, 039902.

Barleon, L., Mack, K.-J. and Stieglitz, R.: 1996, The MEKKA-facility a flexible tool to investigate MHD-flow phenomena, *Technical Report FZKA 5821*, Forschungszentrum Karlsruhe.

Branover, G. G., Gel'fgat, Y. M., Kit, L. G. and Tsinober, A. B.: 1970, Study of MHD turbulence in tubes using conduction anemometers, *Mekh. Zhidk. Gaza* **5**(2), 35–44.

Branover, G. G., Gel'fgat, Y. M., Tsinober, A. B., Shtern, A. B. and Shcherbinin, E. V.: 1966, The application of Pitot and Prandtl tubes in magnetohydrodynamic experiments, *Magnetohydrodynamics* **2**(1), 55–58.

Bühler, L.: 2008, Three-dimensional liquid metal flows in strong magnetic fields, *Technical Report FZKA 7412*, Forschungszentrum Karlsruhe. Habilitationsschrift Universität Karlsruhe.

Bühler, L. and Horanyi, S.: 2006, Experimental investigations of MHD flows in a sudden expansion, *Technical Report FZKA 7245*, Forschungszentrum Karlsruhe.

Bühler, L. and Horanyi, S.: 2009, Measurements of time-dependent liquid metal magnetohydrodynamic flows in a flat rectangular duct, *Fusion Engineering and Design* **84**, 518–521.

Bühler, L., Horanyi, S. and Mistrangelo, C.: 2008, Interpretation of LEVI velocity signals in 3D MHD flows, *Fusion Engineering and Design* **83**(10-12), 1822–1827.

Burr, U.: 1998, *Turbulente Transportvorgänge in magnetohydrodynamischen Kanalströmungen*, PhD thesis, Universität Karlsruhe. Tech. Rep. FZKA 6038, Forschungszentrum Karlsruhe.

Burr, U., Barleon, L., Müller, U. and Tsinober, A. B.: 2000, Turbulent transport of momentum and heat in magnetohydrodynamic rectangular duct flow with strong side wall jets, *Journal of Fluid Mechanics* **406**, 247–279.

Eckert, S., Cramer, A. and Gerbeth, G.: 2007, Velocity measurement techniques for liquid metal flows, *in* S. Molokov, R. Moreau and H. K. Moffatt (eds), *Magnetohydrodynamics Historical Evolution and Trends*, Springer, Dordrecht, pp. 275–294.

Foust, O. J.: 1972, *Sodium - NaK Engineering Handbook*, Gordon and Breach Science Publishers.

Horanyi, S., Bühler, L. and Arbogast, E.: 2005, Experiments on magnetohydrodynamic flows in a sudden expansion of rectangular ducts at high Hartmann numbers, *Proceedings of the Joint 15th Riga and 6th Pamir International Conference, Riga, June 27-July 1*, Vol. 1, pp. 243–246.

Hunt, J. C. R. and Malcolm, D. G.: 1968, Some electrically driven flows in magnetohydrodynamics. Part 2. Theory and experiment, *Journal of Fluid Mechanics* **33**(4), 775–801.

Hunt, J. C. R. and Stewartson, K.: 1969, Some electrically driven flows in magnetohydrodynamics. Part 3. The asymptotic theory for flow between circular electrodes, *Journal of Fluid Mechanics* **38**(2), 225–242.

Kirillov, I., Reed, C. B., Barleon, L. and Miyazaki, K.: 1995, Present understanding of MHD and heat transfer phenomena for liquid metal blankets, *Fusion Engineering and Design* **27**, 553–569.

Kit, L. G.: 1970, Turbulent velocity fluctuation measurements using a conduction anemometer with a three-electrode probe, *Magnetohydrodynamics* **6**(4), 480–484.

Kit, L. G., Kolesnikov, Y. B., Tsinober, A. B. and Shtern, P. G.: 1969, Use of a conduction anemometer in investigating the MHD wake behind a body, *Magnetohydrodynamics* **5**(4), 46–50.

Kolesnikov, Y. B. and Tsinober, A. B.: 1972, Two-dimensional turbulent flow behind a circular cylinder, *Magnetohydrodynamics* **8**(3), 300–307.

Kolin, A.: 1943, Electromagnetic method for the determination of velocity distribution in a fluid flow, *Physical Review* **63**, 218–219.

Kolin, A.: 1944, Electromagnetic velometry. I. A method for the determination of fluid velocity distribution in space and time, *Journal of Applied Physics* **15**, 150–164.

Kolin, A. and Reiche, F.: 1954, Electromagnetic velometry. II. Elimination of the effects of induced currents in explorations of the velocity distribution in axially symmetrical flow, *Journal of Applied Physics* **25**(4), 409–413.

Korsunskii, L. M.: 1975, Measuring capabilities of conduction anemometers with a uniform external magnetic field, *Magnetohydrodynamics* **11**(2), 231–234.

Mistrangelo, C.: 2005, Three-dimensional MHD flow in sudden expansions, *Technical Report FZKA 7201*, Forschungszentrum Karlsruhe. PhD Thesis, University of Karlsruhe.

Morley, N. B., Malang, S. and Kirillov, I.: 2005, Thermofluid magnetohydrodynamic issues for liquid breeders, *Fusion Science and Technology* **47**(3), 488–501.

Patankar, S. V.: 1980, *Numerical Heat Transfer and Fluid Flow*, Hemisphere Publ.Co.

Picologlou, B. F., Reed, C. B., Dauzvardis, P. V. and Walker, J. S.: 1986, Experimental and analytical investigations of magnetohydrodynamic flows near the entrance to a strong magnetic field, *Fusion Technology* **10**, 860–865.

Platnieks, I. and Uhlmann, G.: 1984, Hot-wire sensor for liquid sodium, *Journal of Physics E: Scientific Instruments* **17**(10), 862–863.

Reed, C. B., Picologlou, B. F., Dauzvardis, P. V. and Bailey, J. L.: 1986, Techniques for measurement of velocity in liquid-metal MHD flows, *Fusion Technology* **10**, 813–821.

Ricou, R. and Vives, C.: 1982, Local velocity and mass transfer measurements in molten metals using an incorporated magnet probe, *International Journal of Heat and Mass Transfer* **25**(10), 1579–1588.

Sajben, M.: 1965, Hot wire anemometer in liquid mercury, *The Review of Scientific Instruments* **36**(7), 945–949.

Shercliff, J. A.: 1962, *The Theory of Electromagnetic Flow-Measurement*, XI (Cambridge Engineering Series), Cambridge University Pr.

Stahl-Eisen-Werkstoffblätter (SEW 310): 1992, Physikalische Eigenschaften von Stählen, Verlag Stahleisen Düsseldorf.

Tsinober, A., Kit, E. and Teitel, M.: 1987, On the relevance of potential difference method for turbulence measurements, *Journal of Fluid Mechanics* **175**, 447–461.

Votsish, A. D. and Kolesnikov, Y. B.: 1976, Spatial correlation and vorticity in two-dimensional homogeneous turbulence, *Magnetohydrodynamics* **12**(3), 271–274.

Weissenfluh, T.: 1985, Probes for local velocity and temperature measurements in liquid metal flow, *International Journal of Heat and Mass Transfer* **28**(8), 1563–1574.

Williams, E. J.: 1930, The induction of electromotive forces in a moving liquid by a magnetic field, and its application to an investigation of the flow of liquids, *Proceedings of the Physical Society* **42**, 466–487.